



저작자표시-비영리-동일조건변경허락 2.0 대한민국

이용자는 아래의 조건을 따르는 경우에 한하여 자유롭게

- 이 저작물을 복제, 배포, 전송, 전시, 공연 및 방송할 수 있습니다.
- 이차적 저작물을 작성할 수 있습니다.

다음과 같은 조건을 따라야 합니다:



저작자표시. 귀하는 원저작자를 표시하여야 합니다.



비영리. 귀하는 이 저작물을 영리 목적으로 이용할 수 없습니다.



동일조건변경허락. 귀하가 이 저작물을 개작, 변형 또는 가공했을 경우에는, 이 저작물과 동일한 이용허락조건하에서만 배포할 수 있습니다.

- 귀하는, 이 저작물의 재이용이나 배포의 경우, 이 저작물에 적용된 이용허락조건을 명확하게 나타내어야 합니다.
- 저작권자로부터 별도의 허가를 받으면 이러한 조건들은 적용되지 않습니다.

저작권법에 따른 이용자의 권리는 위의 내용에 의하여 영향을 받지 않습니다.

이것은 [이용허락규약\(Legal Code\)](#)을 이해하기 쉽게 요약한 것입니다.

[Disclaimer](#)

이학박사 학위논문

양전자방출단층촬영을 위한  
네트워크 기반  
고성능 데이터획득 장치

Network based  
High Performance  
Data Acquisition System  
for PET Scanner

2015 년 02 월

서울대학교 대학원  
의과학과 의과학전공  
윤 현 석

A thesis of the Doctor of Philosophy' s degree

Network based  
High Performance  
Data Acquisition System  
for PET Scanner

양전자방출단층촬영을 위한  
네트워크 기반  
고성능 데이터획득 장치

February 2015

The Department of Biomedical Sciences,

Seoul National University

Graduate School

Hyun Suk Yoon

# ABSTRACT

**Introduction:** A network based data acquisition (DAQ) system for positron emission tomography (PET) is developed. PET system with high sensitivity and resolution requires high performance DAQ system since large amount of data are being created. Most DAQ acquisition systems for PET are dedicated to one system in terms of output signal types, interface and channel configurations. Modular system which can adopt different input modules was introduced for easy configuration to receive different types of output signal from various PET systems. Field-programmable gate array (FPGA) based signal processing and data transfer with 1-Gbps Ethernet network was used for high system count rate and scalable system.

**Methods:** The DAQ system is composed of 3 boards, input, ADC and FPGA modules. Each DAQ system can acquire 40 analog signal inputs and 10 trigger inputs from PET system. 10-Gbps network switch is used for data transfer and scalable expansion of DAQ system.

**Results:** The 10-Gbps Ethernet network DAQ system was able to acquire the data from the PET scanner with maximum singles count rate of 57.6 Mcps.

**Conclusions:** A 10-Gbps Ethernet network based data acquisition system designed to acquire signals from various PET systems with high system count rate performance was developed. Scalability from 40 to 10,000 readout channel is possible with use of Ethernet based DAQ system.

-----  
**Keywords:** Positron emission tomography, Data acquisition system

**Student number:** 2008-22004

# CONTENTS

<b>Abstract .....</b>	<b>i</b>
<b>Contents.....</b>	<b>ii</b>
<b>List of figures.....</b>	<b>iv</b>
<b>List of tables .....</b>	<b>vii</b>
<b>List of abbreviations .....</b>	<b>viii</b>
<b>General Introduction .....</b>	<b>1</b>
<b>Chapter 1 .....</b>	<b>3</b>
<b>High Performance Network based Data Acquisition System</b>	
<b>Introduction .....</b>	<b>4</b>
<b>Material and Methods.....</b>	<b>7</b>
<b>Results.....</b>	<b>19</b>
<b>Discussion .....</b>	<b>24</b>
<b>Conclusion.....</b>	<b>26</b>
<b>Chapter 2 .....</b>	<b>27</b>
<b>Analog Bipolar Multiplexing for DAQ Channel Expansion</b>	
<b>Introduction .....</b>	<b>28</b>
<b>Material and Methods.....</b>	<b>31</b>
<b>Results.....</b>	<b>42</b>
<b>Discussion .....</b>	<b>45</b>
<b>Conclusion.....</b>	<b>49</b>

<b>Chapter 3 .....</b>	<b>50</b>
<b>Application to the PET System for Simultaneous PET-MR Imaging</b>	
<b>Introduction .....</b>	<b>51</b>
<b>Material and Methods .....</b>	<b>54</b>
<b>Results.....</b>	<b>63</b>
<b>Discussion .....</b>	<b>68</b>
<b>Conclusion .....</b>	<b>72</b>
<b>References.....</b>	<b>73</b>
<b>Abstract in Korean .....</b>	<b>79</b>

# LIST OF FIGURES

Figure 1- 1 Concept of modular data acquisition system.....	8
Figure 1- 2 Schematic of ADC module.....	9
Figure 1- 3 Simplified schematic of DAQ system .....	10
Figure 1- 4 Diagram of network based scalable DAQ system.....	12
Figure 1- 5 10-Gbps network based scalable DAQ system .....	14
Figure 1- 6 Waveform monitoring using debug module .....	15
Figure 1- 7 Schematic of data acquisition system for TOF application.....	16
Figure 1- 8 Three-layer block detector configuration (a) and diagram DOI PET system (b).....	17
Figure 1- 9 Head to tail charge integration for pulse shape analysis (PSA).....	18
Figure 1- 10 Improvement by baseline correction in the acquisition process.....	19
Figure 1- 11 Count rate performance of 1-Gbps based DAQ system .....	20
Figure 1- 12 Count rate performance of 10-Gbps based DAQ system.....	21
Figure 1- 13 Scalability test of 10-Gbps based DAQ system .....	21
Figure 1- 14 Photograph of 40 channel DAQ system .....	22
Figure 1- 15 Layer separation of 2-layer DOI Detector with PSA .....	23
Figure 1- 16 Tail to head integration value ratio of 3-layer DOI block.....	23

Figure 2- 1 Block diagram of non-multiplexed (left), multiplexed (right) detector configuration .....	29
Figure 2- 2 Sampled pulses of multiplexed position related signals .....	32
Figure 2- 3 Circuit configuration for difference amplifier used in multiplexing. ....	33
Figure 2- 4 Example of 4:1 multiplexing circuit.....	34
Figure 2- 5 Block diagram showing the experimental setup to acquire coincidence data with DRS4 based data acquisition system .....	36
Figure 2- 6 Changes in global average energy resolution (a), global average coincidence resolving time (CRT) (b) and flood histogram quality parameter $k$ (c) of two block detectors in various multiplexing ratios.....	43
Figure 2- 7 Flood histograms and line profile of two block detectors for all multiplexing ratios .....	44
Figure 2- 8 Flood histograms of 16 block detectors multiplexed with 16:1 bipolar multiplexing circuit .....	44
Figure 2- 9 Multiplexing method with differential signaling.....	45

Figure 3- 1 SiPM detector module and shielding box.....	55
Figure 3- 2 MRI-compatible SiPM PET scanner consisting of 12 detector modules .....	58
Figure 3- 3 SiPM PET insert placed outside and inside 3-T MRI scanner Simultaneous PET/MR Imaging.....	58
Figure 3- 4 Flood histograms of SiPM PET detector module acquired without (A) and with (B) application of radiofrequency pulse sequences, and profiles on them. Boxed regions are where profiles were estimated.....	65
Figure 3- 5 T2-weighted MRI scans of uniform cylindrical phantom acquired without (A) SiPM-PET insert and with (B) insert (power on). Circled regions are where signal-to- noise ratio, summarized in Table 3- 4, was estimated.....	66
Figure 3- 6 Simultaneously acquired PET and MRI (T2-weighted turbo spin echo) scans of three $^{18}\text{F}$ -filled capillary tubes inserted into cucumber. ....	67
Figure 3- 7 In vivo PET/MRI (T2-weighted turbo spin echo) study in BALB/c mouse after injection of $^{18}\text{F}$ -FDG.....	67

## LIST OF TABLES

Table 2- 1. Polarity combination table for bipolar multiplexing.....	35
Table 3- 1 Specification of SiPM (MPPC S11064-050P) .....	55
Table 3- 2 Major characteristics of MRI-compatible SiPM PET ....	57
Table 3- 3 Peak-to-valley ratio along profiles on middle rows in flood histograms shown in Figure 3- 4 .....	65
Table 3- 4 Summary of average signal intensity and signal-to-noise ratio of MRI scans shown in Figure 3- 5.....	66

## LIST OF ABBREVIATIONS

---

<b>Full Name</b>	<b>Abbreviations</b>
<b>Analog to Digital Converter</b>	ADC
<b>Avalanche Photodiode</b>	APD
<b>Application Specific Integrated Circuit</b>	ASIC
<b>Block Detector Processing Module</b>	BDPM
<b>Constant Fraction Discriminator</b>	CFD
<b>Coincidence Resolving Time</b>	CRT
<b>Computed Tomography</b>	CT
<b>Data Acquisition</b>	DAQ
<b>Depth of Interaction</b>	DOI
<b>Digital Signal Processing</b>	DSP
<b>First-in, First-out</b>	FIFO
<b>Field Programmable Mezzanine Card</b>	FMC
<b>Field of View</b>	FOV
<b>Field Programmable Gate Array</b>	FPGA
<b>I/O Completion Port</b>	IOCP
<b>Leading Edge Discriminator</b>	LED
<b>Low Voltage Differential Signal</b>	LVDS
<b>Multi-Anode Photomultiplier</b>	MA-PMT

<b>Multipixel Photon Counter</b>	MPPC
<b>Magnetic Resonance Imaging</b>	MR(I)
<b>Positron Emission Tomography</b>	PET
<b>Photomultiplier Tube</b>	PMT
<b>Pulse Shape Analysis</b>	PSA
<b>Charge to Digital Converter</b>	QDC
<b>Resistive Charge Division Network</b>	RCN
<b>Silicon Photomultiplier</b>	SiPM
<b>Single Photon Emission Computed Tomography</b>	SPECT
<b>Time to Digital Converter</b>	TDC
<b>Time of Flight</b>	TOF
<b>User Datagram Protocol / Internet Protocol</b>	UDP/IP

---

# GENERAL INTRODUCTION

Positron emission tomography (PET) imaging system is widely used for non-invasive function and molecular imaging of various sized subjects, from small animals to human whole-body. To meet the needs of different application in terms of object size, various PET system have been developed. Typically, PET system consists of a large number of radiation block detector modules which detects positron emitted gamma photons, front electronics that receive and amplify the signal from detector module, a data acquisition (DAQ) system that acquires and processes the detected gamma-ray events and a computer for image reconstruction.

Other gamma or X-ray imaging modalities; such as gamma camera, single photon emission computed tomography (SPECT) or x-ray computed tomography (CT), have a small number of detector modules compare to PET system and images are reconstructed based on single events. Therefore signals can be processed in the early stage of data paths and reduces large amount of data by extracting and filtering only essential information.

In contrast, PET reconstructs tomographic images based on coincidence of two gamma-rays. To resolve the coincidence of two gamma-rays from positron-electron annihilation, which are detected at two arbitrary detectors, the data of all detected gamma-ray events need to be passed over through the data path to the point, where the events from all detector modules are gathered. Furthermore, PET systems have a large number of detector modules so a large amount of data is detected compared to other modalities. Count rate performance, one of key performance parameter of the PET system, is determined by how DAQ system

handles acquisition and processing of such incoming data.

Recently, development of PET detectors with high sensitivity and resolution [1–3] and new approach of total body scanner with tunnel-like scanner geometry [4] increased needs for the DAQ systems with higher density readout channels and count rate processing capabilities.

The aim of this thesis is to develop DAQ system which is designed to use for various PET systems from small animal to clinical human whole body scanner. In Chapter 1, a network based high performance DAQ system for PET scanners was developed. Multi-channel readout with scalability and high count rate performance were achieved using free running analog to digital converters (ADCs) and field-programmable gate array (FPGA). The function and performance of DAQ system will be presented. In Chapter 2, an analog bipolar multiplexing was developed for expansion of DAQ system. A novel multiplexing method to efficiently reduce the number of required readout channels without modifying the DAQ system will be presented. Finally in Chapter 3, a small animal PET scanner which is capable of PET-MR simultaneous with proposed DAQ system and multiplexing method was developed. Phantom and animal studies were performed to verify the functionalities of DAQ system.

# **CHAPTER 1**

## **High Performance Network based Data Acquisition System**

# INTRODUCTION

In general, a PET system's performance; spatial resolution and sensitivity, is maximized when the scanner gantry diameter is small as possible due to annihilation photon non-collinearity and geometric efficiency [5]. Therefore it is required to design an optimized and dedicated PET system to achieve required spatial resolution and size of field-of-view (FOV) of each imaging subject. Especially, dedicated data acquisition (DAQ) system needs to be designed for a specific detector type and number of detectors [6–8].

Tradition DAQ systems for PET scanner were based on charge integration method (i.e. charge-to-digital-converter, QDC) for obtaining energy and position information of the detected gamma events. However this kind of data acquisition method loses most of the detected information and has difficulties of post-acquisition signal processing such as baseline shift correction or pulse shape analysis. Therefore such system needs addition analog circuits prior to acquisition and these circuits made the system complex and big.

With recent development of high speed sampling analog-to-digital-converters (ADC), acquisition of detected events preserving information for post-acquisition process became possible. Sampled pulse information enables various post acquisition signal processing (i.e. baseline correction and pulse shape analysis) and reduces analog circuits for corrections. But pulse sampling of the detected events with ADCs increases amount of data by ten- to hundred-fold as compared to QDC based acquisition system and these amount of data processing is not for PET application since data transfer speed and signal

processing power are limited.

Use of separate signal processing device such as application-specific integrated circuit (ASIC), digital signal processing (DSP) and field-programmable gate array (FPGA) made sampling DAQ system for PET application possible. Such devices do not have high processing power compare to computers, however real-time signal processing is possible with parallel signal processing architecture of these devices, which distributes the signal processing and process them simultaneously. Signal processing of the detected events reduces the amount of data to be transferred to acquisition computer by extracting and only required information; therefore higher count rate can be achieved with same data transfer speed.

There are various PET block detectors in terms of output signal characteristics, output impedance, signal dynamic range and output connector types which are determined by the type of photo-sensors in use and front electronics that match system requirements. To be able to correspond to various PET scanners with different output characteristics while sharing essential part of DAQ system (i.e. ADC, FPGA), modular DAQ system is proposed.

In this study, we propose two types of DAQ system. One is single block DAQ system, which is designed to use separate DAQ board for each block detector. With this DAQ system, a DAQ board can be integrated into a block detector module for minimizing wiring density and analog signal transfer length. The other type is multi block modular DAQ system. A multichannel DAQ system which is designed to acquire and process 10 to 160 block detectors. Flexible modular structure is introduced for handling PET scanners with different

detector output signals while using common base modules. Both DAQ system are developed with following key points.

- Network based scalable DAQ system for various number of block detectors. PET is widely used for molecular imaging of various sized subjects, from small animals to human whole-body. Required spatial resolution and size of FOV varies with the subject.
- Waveform sampling based DAQ system with high-speed, free-running ADCs and FPGA for waveform based signal processing.
- High count rate system with the use of fully digital parallel and pipelined signal processing using programmable logic device.
- Singles list-mode based acquisition system. All data acquisition parameter of interest can be adjusted with post-acquisition processing, generating different images with different data acquisition parameter (energy threshold, coincidence timing window, coincidence detection/rejection algorithm, random correction) from singles acquired in a single scan [9].

# MATERIALS AND METHODS

## 1. Single block data acquisition system

The single block data acquisition system is equipped with DAQ boards, a master board, and an acquisition computer. Each DAQ board consists of one FPGA and five free-running ADCs. Five ADCs on a DAQ board digitize position-dependent PET signals from a detector module at a 170-MHz sampling rate with a resolution of 12 bits (AD9430, Analog Devices). The digitized signals are processed with the FPGA (Xilinx Spartan 3A DSP, Xilinx). With an external trigger, such as a leading edge discriminator (LED) or constant-fraction discriminator (CFD), the FPGA acquires samples (number of samples varies depend on output pulse length) for energy and position calculation. Prior to the trigger, one to 20 samples are used for baseline correction of each event. Because these calculations are processed by the FPGA with a pipeline structure, no extra dead time is caused by the calculation. Finally, the FPGA sends out a data package of an event to the master board at a data rate of 350 Mb/s via a low-voltage differential signaling (LVDS) transmitter.

The FPGA-based master board (Xilinx Virtex 5, Xilinx) receives the data from DAQ boards and logically processes the coincidence events with a coincidence window of 2 ns [53]. The coincidence events are then transferred to the PC via 1-Gbps Ethernet.

## 2. Multi block modular DAQ system

The architecture of proposed multi block modular DAQ system is shown in Figure 1- 1. The system is consisted of input, ADC and FPGA boards. The input board corresponds to different PET system and rest of boards can be used without any modifications.

The ADC board accepts differential signals with input voltage range of 2 V, therefore the input module needs to convert the signals from PET system if transferred signals are single-ended. Two types of input board are developed, one accepts single-ended input and other accepts differential input signals. Both input boards support 40 signal inputs and 10 external trigger input. The single-ended input board converts single-ended signal to differential signal using active amp, therefore it is possible to amplify the signals if needed (Figure 1- 1).

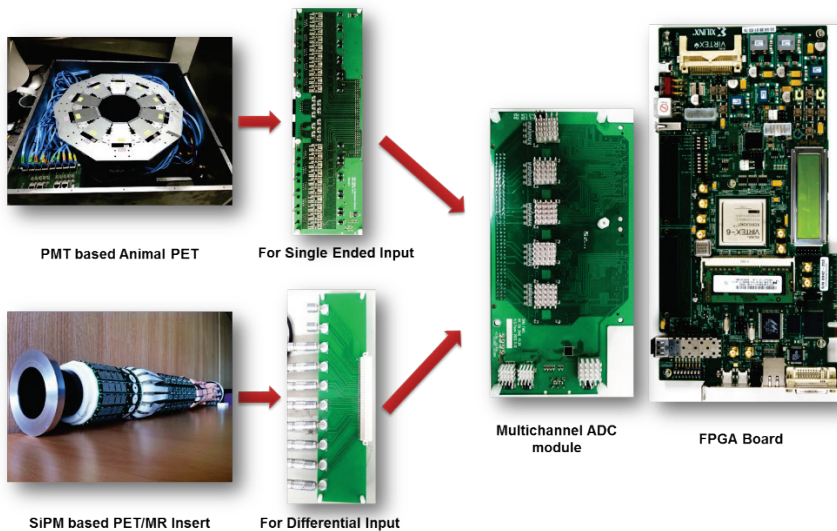


Figure 1- 1 Concept of modular data acquisition system

The ADC board is composed of 10 quad channel free-running analog to digital converters(ADCs) with 12 bit voltage resolution and 125 MHz sampling frequency (ADS6425, Texas Instruments), which makes total of 40 channels.

The ADC board accepts 40 differential analog signals with differential input range of 2 Volts-peak-to-peak and 10 external trigger signals with low voltage differential signal (LVDS) specification. The external trigger signals are bypassed to the FPGA board directly. The digitized signals from ADCs are sent to FPGA board with serialized LVDS lines. For each channel, serialized data are sent over two LVDS pairs with rate of 750 Mbps ( $12 \text{ bit} \times 125 \text{ Msamples/sec} / 2$ ). Sampling reference clock to drive ADCs are fed from FGPA board and buffered with 1:10 clock buffer to synchronize the sampling of all 40 channels (Figure 1- 2)

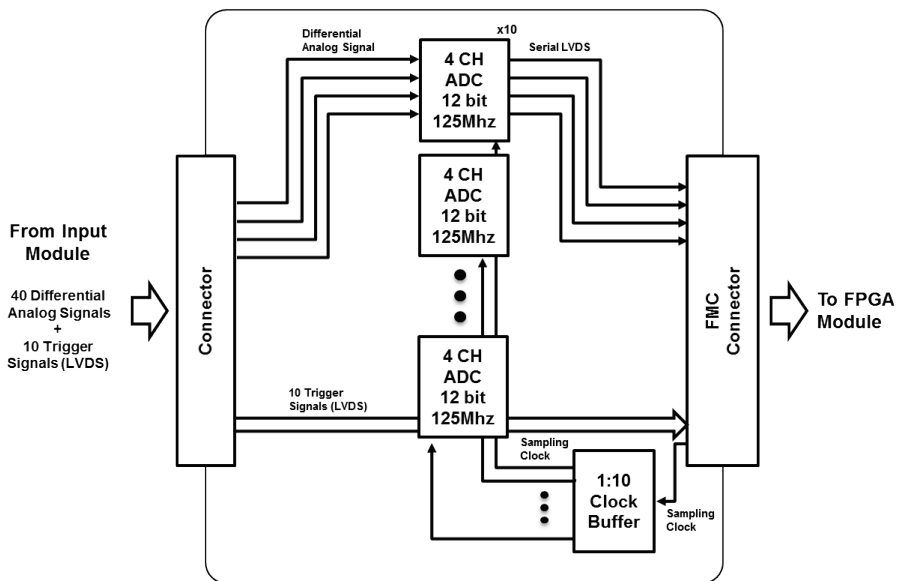


Figure 1- 2 Schematic of ADC module

Field programmable mezzanine card (FMC) standard connectors (one high pin count [HPC] and one low pin count [LPC] connectors) are used to send sampled data to FPGA board. With use of standard connectors, the ADC board is compatible to different commercially available FPGA boards.

The FPGA board acquires the digitized signal from ADCs in the ADC board and processes the signal. The board has a Xilinx Virtex-6 FPGA which runs on 125MHz on-board clock for signal processing and 500MHz clock for the time stamp with timing resolution of 2 ns. A FPGA module can accept 40 channels of digitized signals from ADCs and 10 external trigger inputs simultaneously. Commercial evaluation board from Xilinx was used for FPGA module (Virtex 6 ML605 Evaluation board, Xilinx) (Figure 1- 3)

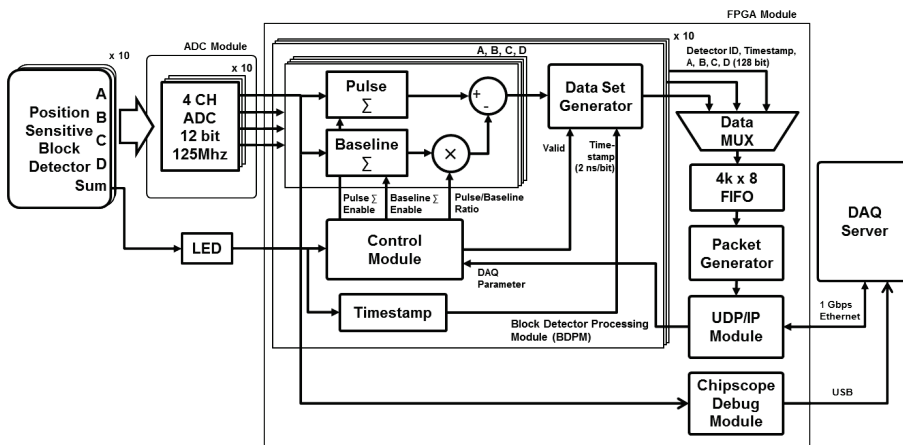


Figure 1- 3 Simplified schematic of DAQ system

### 3. Signal processing and data transfer

For every block detectors, a block detector processing modules (BDPM) within FPGA acquires and processes 4 position related signals. Control module in the BDPM accepts an external trigger signal from a block detector and starts internal signal processing. The pulse and baseline integration of 4 position related signals are individually processed. The integration width and timing are controlled by the control module. Signal processing in the BDPM are designed with parallel and pipelined structure for high speed count rate performance. The parameters for the control module are configurable through Ethernet.

Baseline correction before the pulse integration is essential to minimize the variation of energy and position caused by baseline shift. For every event, 1 to 255 samples (typically 8 samples) prior to the pulse are integrated to get baseline offset value for each event. The integrated value of baseline is subtracted from the pulse integration value with factor of pulse and baseline integration width ratio.

For each singles event, the BDPM generates 128 bit dataset: 8 bits for detector ID, 32 bits for timestamp (2 ns/bit for non TOF mode and 1 ps/bit for TOF mode), 16 bits for each position related integrated value (A, B, C and D : total 64 bits) and 24 bits are reserved for future use. Valid singles dataset (128 bit) from each BDPM are read out with round robin method (read cycle: 80 ns), and these singles are multiplexed to  $4096 \times 8$  bit first-in-first-out (FIFO) (write/read cycle: 8 ns; max. 125 MB s<sup>-1</sup>). When 80 singles (1280 bytes) are gathered in the FIFO, a packet is generated and transferred to user datagram protocol/internet protocol (UDP/IP) communication module. The

communication module converts data to UDP/IP packet and transfers the packet to acquisition server via 1-Gbps Ethernet.

With use of UDP/IP for data transfer protocol and standard 1-Gbps network switch, up to 250 FPGA modules (10,000 readout channels) can be connected into a single network and the data from FPGA boards can be transferred to acquisition sever (Figure 1- 4)

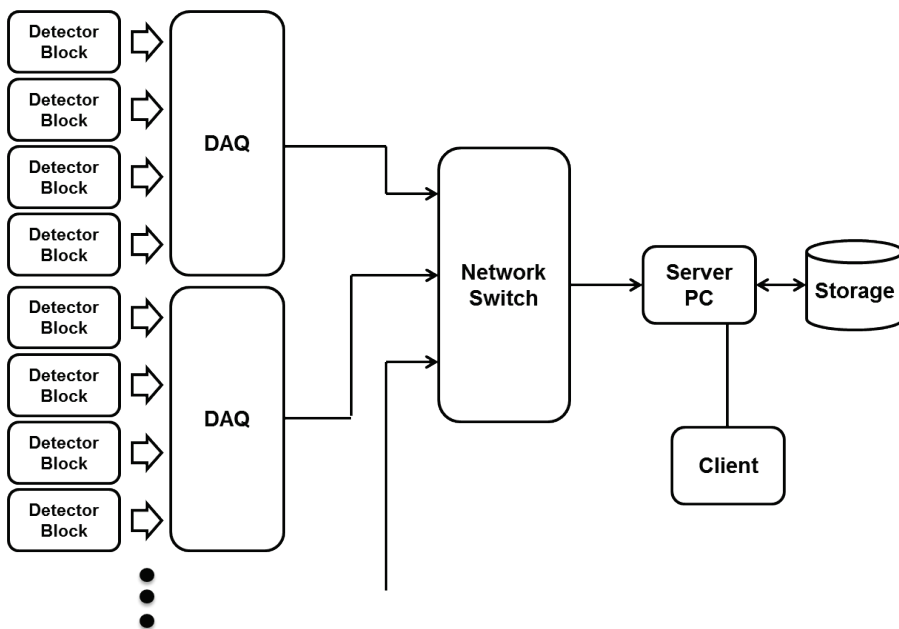


Figure 1- 4 Diagram of network based scalable DAQ system

#### **4. Network based scalable data acquisition system**

Prototype of network based data acquisition system with scalability is composed of multiple DAQ boards with 1-Gbps Ethernet link, an 8-port 10-Gbps Ethernet switch (XS708E, NETGEAR) and a DAQ server (i7-4790 (Intel), 3.6 GHz, 16 GB DDR3, 64 bit Windows 7) with 10-Gbps optical fiber network card (X520-SR, Intel) (Figure 1- 5). The Ethernet switch gathers events from the DAQ boards and uplinks the data to DAQ server through 10-Gbps optical fiber (10GBASE-SR). In order to handle the high data rates the server is equipped with two SSD (256 GB each) in raid 0 configuration.

Two types of acquisition software, programmed with Visual Studio C++, were tested. One with single thread non-blocking socket receiving routine and the other with I/O completion port (IOCP) and multi-thread receiving routine.

Scalability test were performed by one to five computers that generates packets at various count rates. The computers with 1-Gbps Ethernet link were connected to 10-Gbps network switch and the data were transferred to DAQ server.

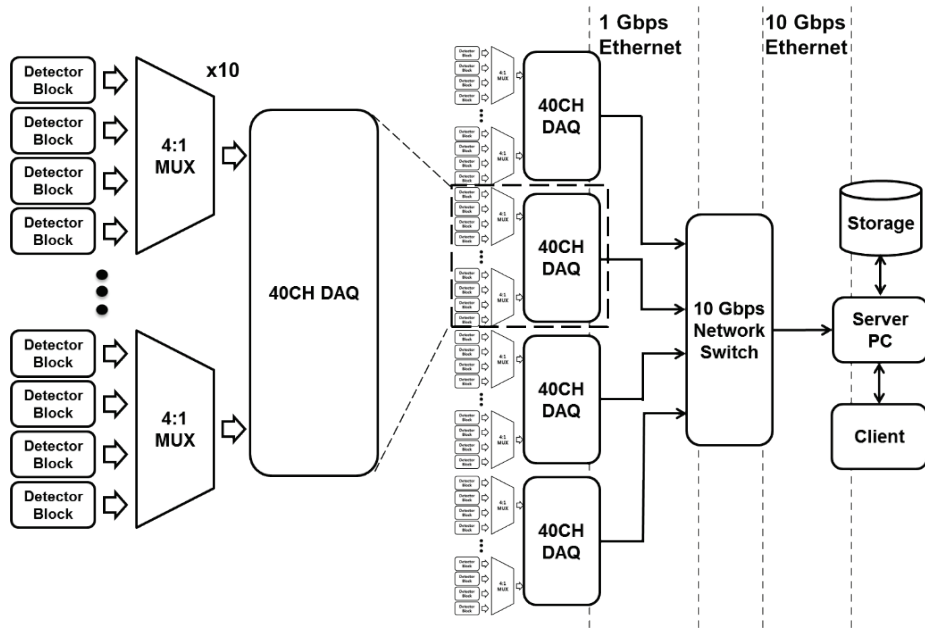


Figure 1- 5 10-Gbps network based scalable DAQ system

## 5. Debug and pulse monitoring module

Since only processed dataset are sent to the acquisition server, the information about the acquired waveform is lost. For the debugging purpose, the sampled waveform can be monitored using debug module as shown in Figure 1-4. The debug module is using Xilinx Chipscope™ technology and is able to monitor all sampled waveform at once. The debug data is sent to data acquisition server via USB (Figure 1- 6).

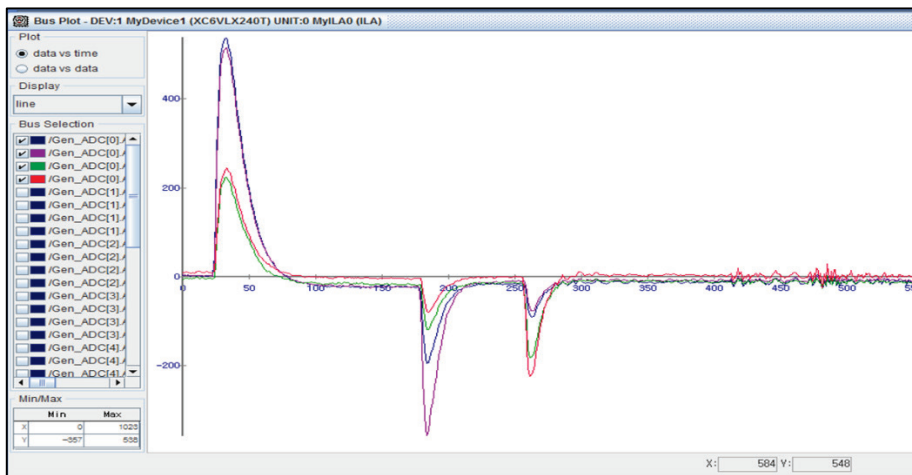


Figure 1- 6 Waveform monitoring using debug module

## 6. Time-of-Flight capability

Timestamp within the DAQ system is supplied at a resolution of 2 ns (500 MHz clock frequency), which is not sufficiently fine for time-of-flight applications. Using external time to digital (TDC) module, timestamp with resolution of 20 ps RMS can be acquired. For every single event total 30 bits dataset, 8 bits for block detector ID and 24 bits for fine timestamp data (1 ps/bit), is received using Xilinx GTX data transfer protocol (Figure 1- 7).

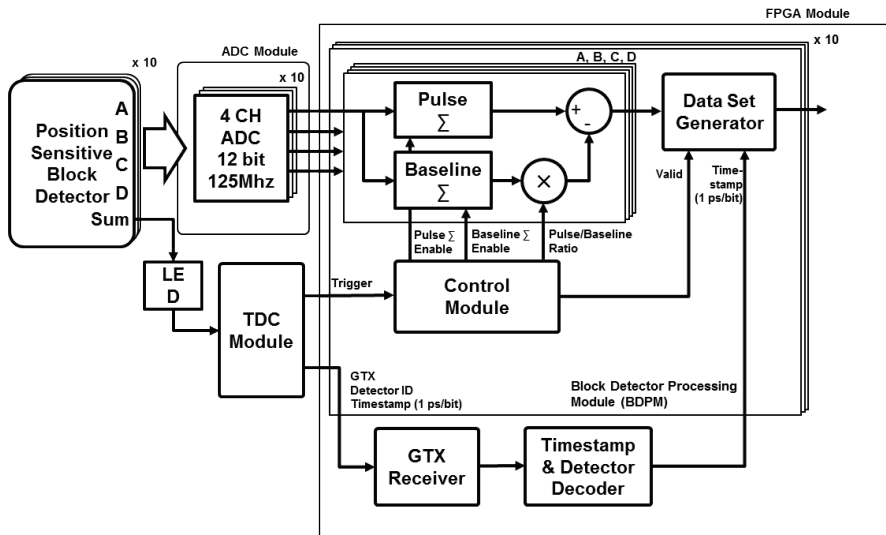


Figure 1- 7 Schematic of data acquisition system for TOF application

## 7. Pulse shape analysis for DOI detector

The 3 layer depth-of-interaction (DOI) PET system (Figure 1- 8) is used to verify pulse shape analysis (PSA) processing for DOI PET detector. A detector module is consisted of one layer of the  $L_{0.2}$ GSO crystal array and two layers of the  $L_{0.9}$ GSO crystal arrays and with the crystal dimension of  $1.5 \times 1.5 \times 7 \text{ mm}^3$ .  $L_{0.2}$ GSO crystal layer and  $L_{0.9}$ GSO crystal layer in the middle is aligned and the top  $L_{0.9}$ GSO crystal layer is placed with the offset of half a crystal pitch in x- and y- directions to the other two crystal layers.  $L_{0.2}$ GSO crystal layer is attached to the surface of Hamamatsu H9500 multi-anode photomultiplier [10].

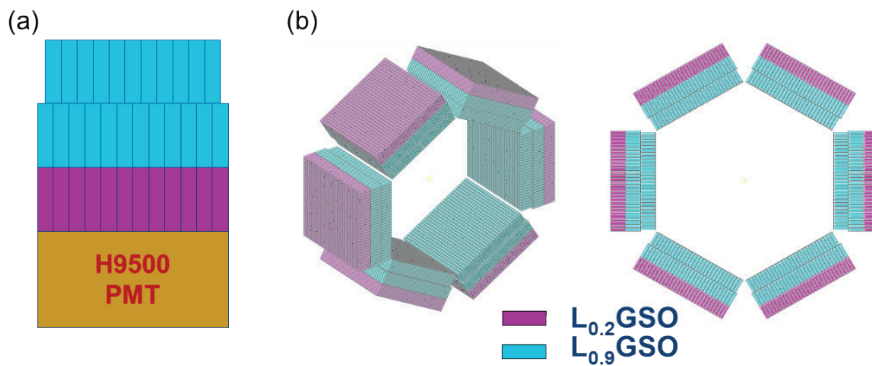


Figure 1- 8 Three-layer block detector configuration (a) and diagram DOI PET system (b)

The dynode signal of photomultiplier is sampled with free running Analog-to-Digital Converter running at 170 mega-samples per sec (MSPS) for pulse shape analysis. For the real-time crystal identification capability, the sampled signals is processed with Xilinx Spartan 3A DSP. Baseline shift of dynode signal is compensated with value of few samples before event. The external constant fraction discriminator triggers the FPGA for analysis of each event.

For the DOI information, the relative offset method is used for discriminating the front & middle layers, the pulse shape discrimination method is used for the  $L_{0.2}$ GSO &  $L_{0.9}$ GSO crystal layers

Head to tail charge integration method is used for PSA and it uses the integrated values of the head and tail part of the pulse. Each integration widths are optimized to  $L_{0.2}$ GSO20 and  $L_{0.9}$ SGO crystal characteristics (Figure 1- 9).

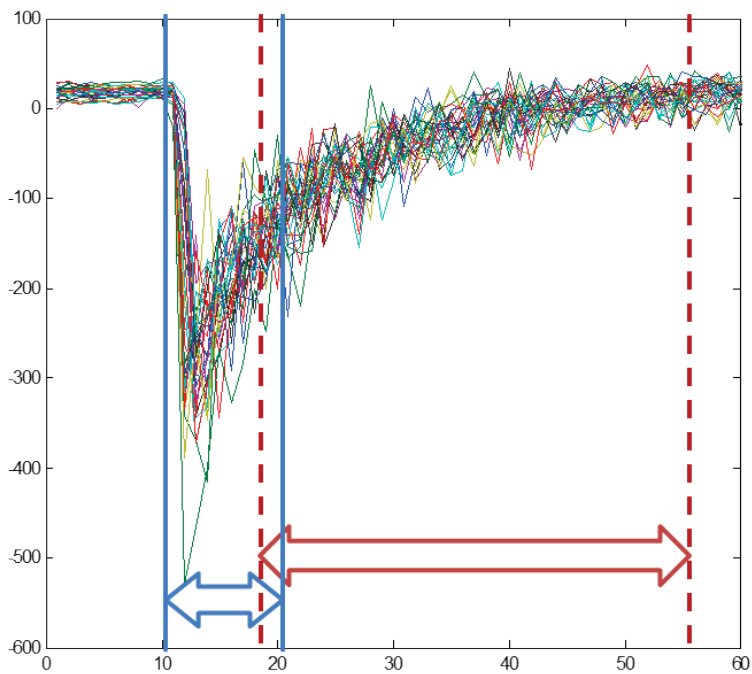


Figure 1- 9 Head to tail charge integration for pulse shape analysis (PSA)

# RESULTS

Energy resolution and flood histogram quality with and without baseline correction were compared (Figure 1- 10). With baseline correction, the energy resolution was improved from 26.5% to 19.6% and crystal peaks in the flood histogram were separated better (Figure 1- 10 (b) and (c)).

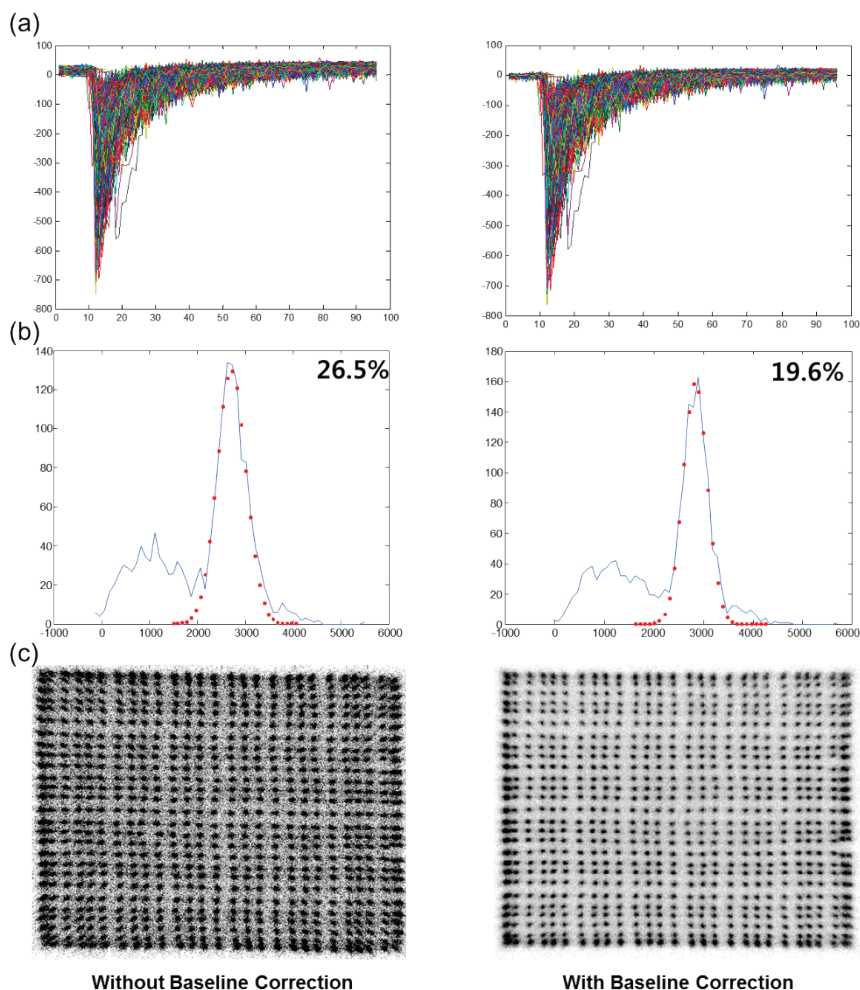


Figure 1- 10 Improvement by baseline correction in the acquisition process (a) Effect on sampled waveform (b) Energy resolution improvement (c) Flood histogram improvement

System count rate performance of 1-Gbps based DAQ system was measured by feeding signals of varying frequency from the pulse generator into external trigger input. Events created by test pulse were transmitted from DAQ system to acquisition computer with maximum count rate of 7Mcps and to disk with maximum count rate of 6.3 Mcps with C++ based acquisition software (Figure 1- 11).

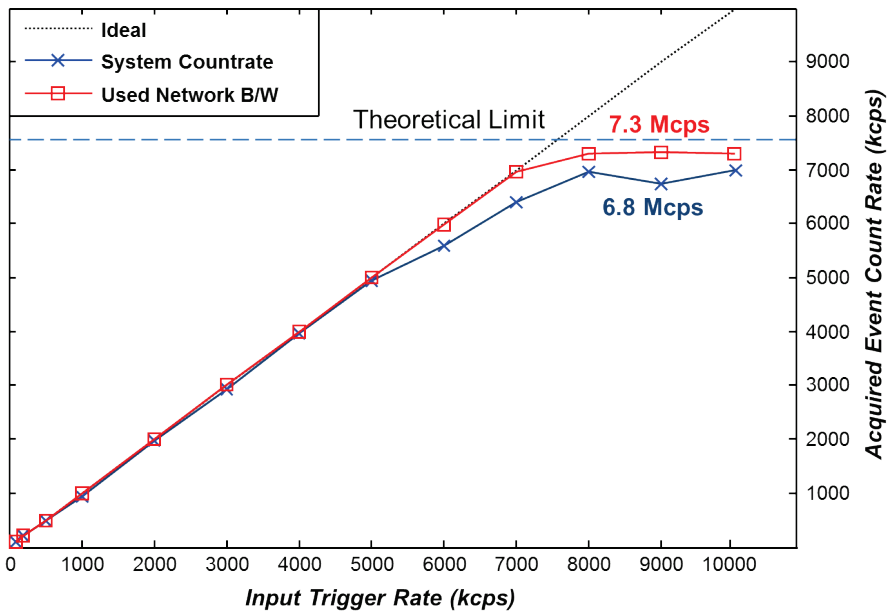


Figure 1- 11 Count rate performance of 1-Gbps based DAQ system

Count rate performance of 10-Gbps based DAQ system was measured with two types of acquisition software. Single-thread non-blocking acquisition routine showed count rate of 27.3 Mcps and multi-thread with IOCP based acquisition software showed count rate of 57.6 Mcps (Figure 1- 12). Scalability of the DAQ system was tested by attaching one to five packet generating nodes to 10-Gbps Ethernet switch (Figure 1- 13). Each node transmits emulated packets at various count rates via 1-Gbps Ethernet to DAQ server.

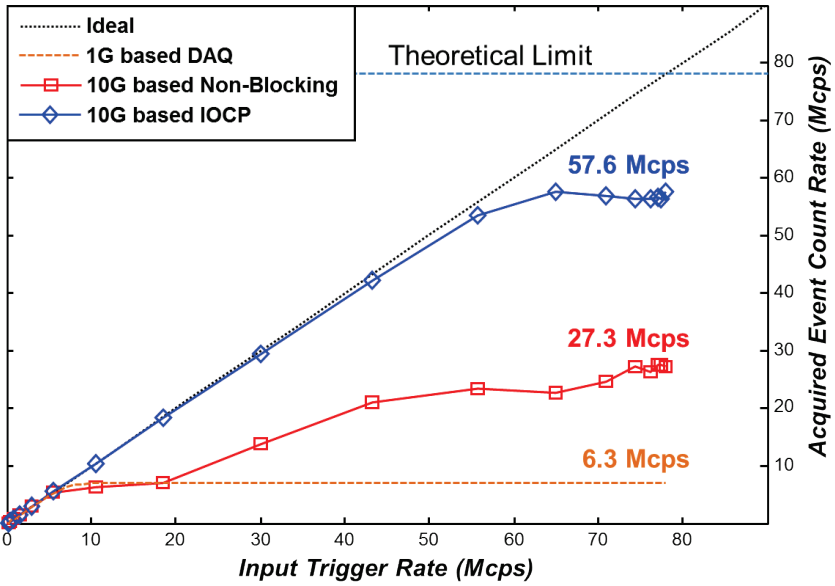


Figure 1- 12 Count rate performance of 10-Gbps based DAQ system

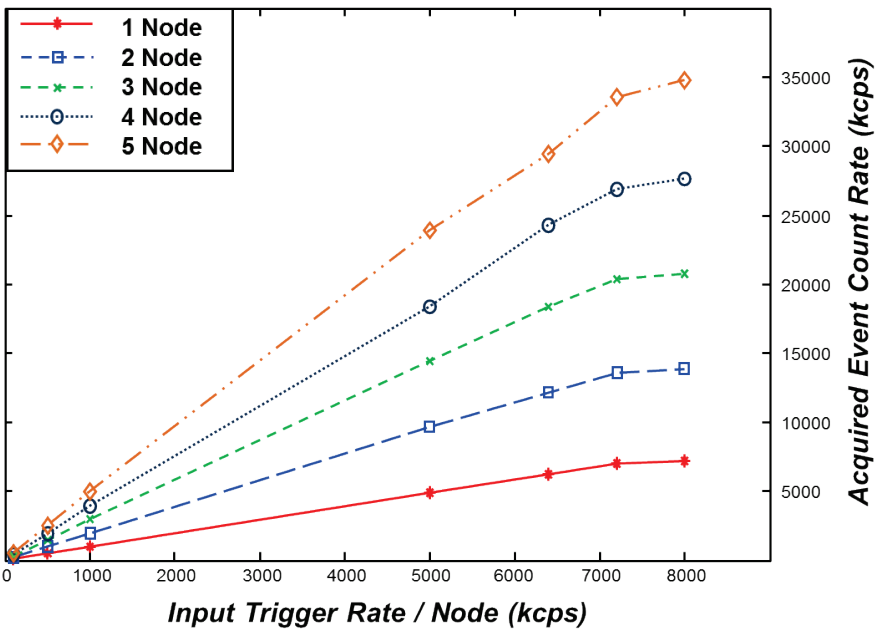


Figure 1- 13 Scalability test of 10-Gbps based DAQ system

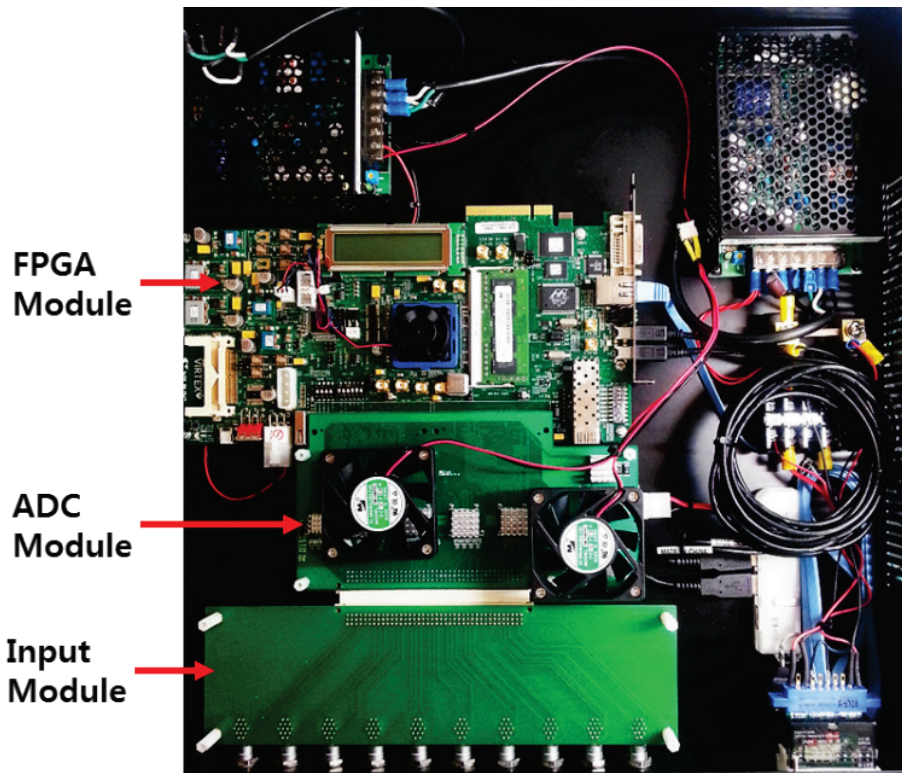


Figure 1- 14 Photograph of 40 channel DAQ system

The PSA signal processing was verified with DOI block detector (Figure 1- 8). To evaluate DOI accuracy of pulse shape discrimination methods, a collimated silt source of  $^{22}\text{Na}$  was placed to illuminate specific layer. For this experiment, the events were acquired in time coincidence with a second detector. With coincidence, the background activity of  $^{176}\text{Lu}$  is suppressed and therefore the signal-to-noise ratio is increased. Figure 1- 15 shows layer separation of 2 layer detector configuration with PSA signal processing. With 3 layer DOI detector, two types of crystal was identified with PSA (Figure 1- 16).

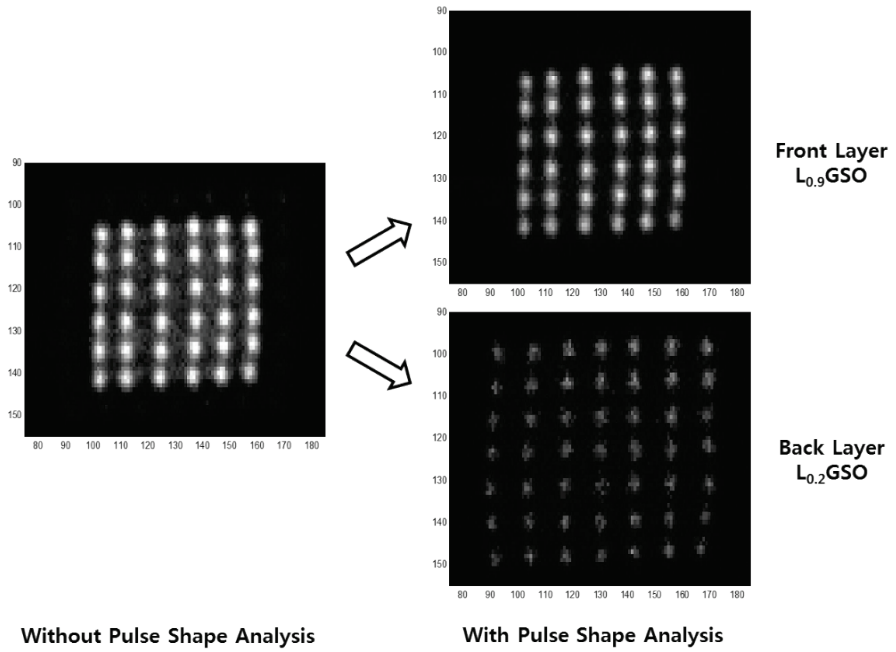


Figure 1- 15 Layer separation of 2-layer DOI Detector with PSA

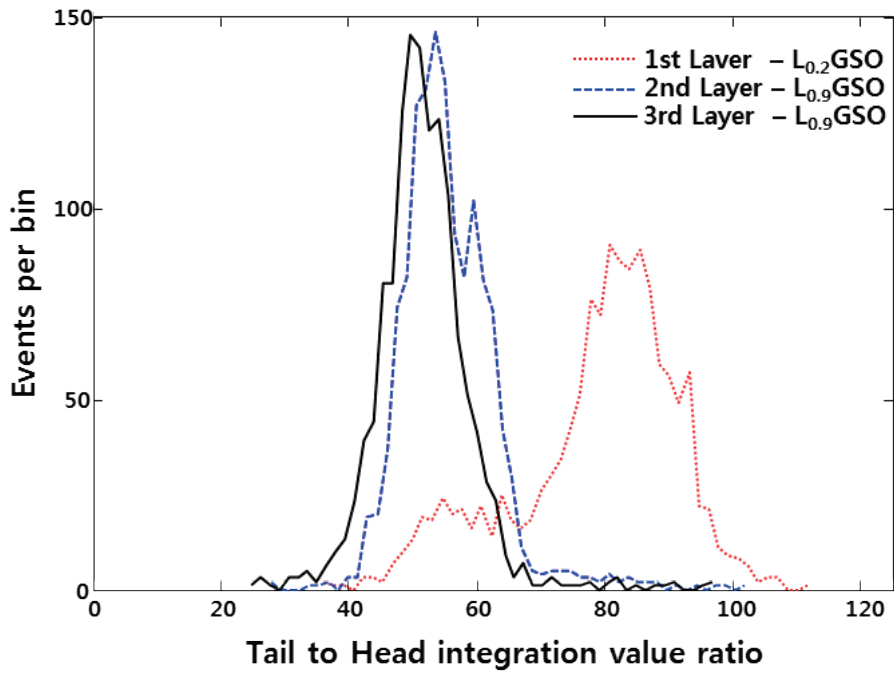


Figure 1- 16 Tail to head integration value ratio of 3-layer DOI block

## DISCUSSION

There are two main factors that limit count rate performance of the DAQ system. One is width of the pulse generated by detectors and the other is limited data transfer rate of the network interface. As internal signal processing in the BDPMs shows non-paralysis nature, the maximum throughput of the BDPMs is determined by the integration width of the pulse. It is possible to achieve higher throughput with implement of analog shaping circuit to reduce the width of pulse [11]. Another possible approach is to implement pulse pile-up recovery method [12] into the internal signal processing into BDPM.

Even though throughput of each module is not saturated, it is possible that count rate of the DAQ system is saturated, as count rates of all the singles datasets from the modules exceed the network bandwidth. Currently 128 bits are used for a single event for preserving data of all readout channels. However, data of all channels are not necessary after optimization of signal processing. Therefore higher count rate performance can be achieved by reducing the size of single dataset with more internal signal processing such as position calculation and crystal identification.

Scalability of DAQ system is important for large scale PET scanner, since design of a single DAQ board to process whole scanner is not efficient. Typically, a DAQ system is composed of multiple DAQ boards to acquire and process output signals locally and data are transferred and gathered through high-speed links.

There two main topology of interconnecting DAQ boards, “tree” [7, 8, 13,

14] and “daisy-chained” [15, 16]. The tree interconnection topology are use conventionally to collect singles from each DAQ board and gathered singes with a coincidence board. However, all singles from DAQ boards are concentrated to a coincidence boards which creates coincidence processing burden and data transfer bottleneck.

In contrast, in the daisy-chained interconnection method, singles generated by each DAQ board are sent to next neighboring board and processing of coincidence is distributed evenly over DAQ boards. For coincidence resolving DAQ system, the daisy-chained topology is efficient in terms of throughput of coincidence events and scalability [16]. However, for single event processing DAQ system, the tree interconnection topology is suitable compare to daisy-chained, since amount of data are accumulated as data are passed through boards in the daisy-chained topology.

## CONCLUSION

A 10-Gbps Ethernet network based DAQ system designed to acquire signals from various PET systems with high system count rate performance was developed. The DAQ system is able to send out single list data with count rate of 57.6 Mcps with C++ based software, which is limited by data processing within device driver of network interface. Theoretically, it is possible to handle up to 160,000 position sensitive block detector with use of analog bipolar multiplexing and expansion through network.

## **CHAPTER 2**

### **Analog Bipolar Multiplexing for DAQ**

#### **Channel Expansion**

# INTRODUCTION

In positron emission tomography (PET), high scanner detection efficiency is required for assuring reliable image quality with a low radiation dose and a short scanning time. When the spatial resolution of a PET scanner is improved, the scanner's sensitivity also needs to be improved to maintain the counting statistics and image quality [17, 18, and 19]. Temporal resolution of PET system, which is affected by the count rate related with the scanner's sensitivity, is important for measuring the dynamics of specific biological processes [19]. In addition, better timing resolution of PET detectors assures the improvement of image quality by rejecting more random counts and incorporating time-of-flight information in PET reconstruction [20, 21]. Accordingly, there have been continuing efforts for developing better PET detectors with high spatial resolution, fast timing resolution and high detection efficiency [1–3]. In many recent investigations for improving PET performances, high density photo-sensors, such as multi-anode photomultiplier tube (MA-PMT) and array-type silicon photomultiplier (SiPM), are used to fulfill the high spatial resolution and fast timing performance [2]. However use of such high density photo-sensor leads to increment of output signal channels in comparison with the conventional PET scanners using head-on type single-channel PMTs.

Moreover, increased axial field-of-view (FOV) of PET scanner by incorporating additional detector rings assures the improvement in the solid angle coverage and hence the overall sensitivity [22, 23]. A potential way to approach the limit of PET sensitivity is the total body scanner with tunnel-like

scanner geometry [4]. However, the extension of axial PET FOV by adding more detector rings requires additional power, cost and space-consuming readout systems. One of the efficient ways to overcome this problem is to multiplex neighboring block detectors, which are not in coincidence, into several blocks before digitizing the output signals (Figure 2- 1).

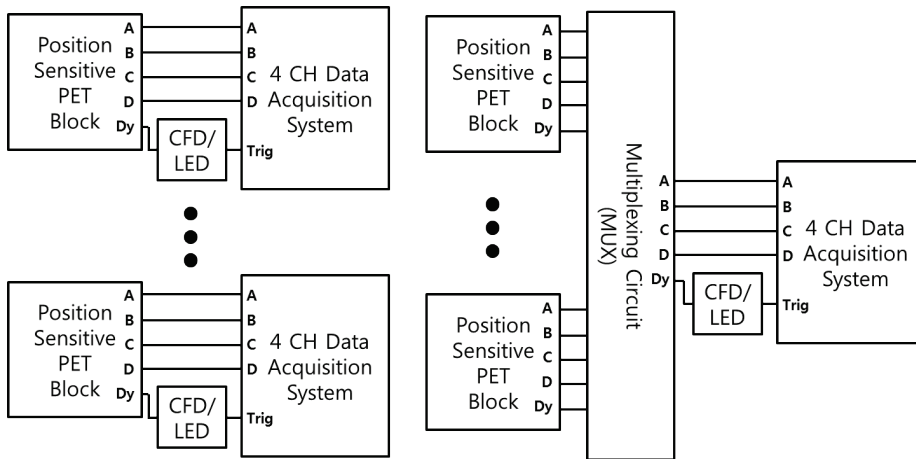


Figure 2- 1 Block diagram of non-multiplexed (left), multiplexed (right) detector configuration

Currently most used multiplexing methods can be categorized into two ways, one of them is Anger-like logic and resistive or capacitive charge-division based multiplexing methods which reduces multiple outputs of photo-sensors into 4 position sensitive signals [24–27]. Gain non-uniformity correction methods can be easily incorporated in these approaches [26, 28]. The other method is that the output signals from multiple detectors share readout channel and the detectors are distinguished using un-multiplexed trigger signals from the detectors [29]. However, the large scale extension of former type of multiplexing method has the limitation because the increased number of input

channels to the multiplexer leads to the output pulse dispersion due to increased RC constant and the reduction of spatial dynamic range in flood histogram map. The latter type of multiplexing method requires additional un-multiplexed trigger signals which need more input channels in subsequent data acquisition (DAQ) system.

Therefore, in this study, we propose an alternative analog signal multiplexing method for position sensitive PET block detectors which does not require additional input trigger channels to DAQ system. The cost of multiplexing analog signal is the information loss and distortion and subsequent degradation of count rate performance mainly due to the higher pulse pile-up. Thus we evaluated the potential degradation of the block detector performance, such as crystal separation, energy resolution and timing resolution, at various multiplexing ratios and count rate conditions. Although this study is focused to PET application, the method can be applied to other applications, which uses position sensitive block detector that gives out single polarity pulses.

# MATERIALS AND METHODS

## 1. Block detector and reference detector configuration

The block detectors used in this study consists of a crystal array, a MA-PMT and readout electronics. The crystal array consists of a  $26 \times 26$  polished lutetium gadolinium oxyorthosilicate ( $\text{Lu}_{1.9}\text{Gd}_{0.1}\text{SiO}_4\text{:Ce}$ , LGSO; Hitachi Chemical, Japan) scintillation crystal with dimension and pitch of  $1.5 \times 1.5 \times 7 \text{ mm}^3$  and 1.65 mm respectively. The crystal arrays are assembled using reflector grid (Enhanced spectral reflector polymer, thickness 0.065 mm; 3M, USA) and optically coupled to 64 channel MA-PMT (H8500; Hamamatsu Photonics, Japan) using optical grease (BC-630, index of refraction: 1.465; Saint-Gobain, France).

The readout electronics consists of anode gain compensation circuits to compensate non-uniform anode gains of MA-PMT [28], a resistive charge division network (RCN) circuit to encode 64 signals into 4 position related signals (A,B,C and D), [30] and an amplifier circuit to amplify 4 position related signals and one dynode signal. Total of 16 block detectors are used in this study, high voltage ranging from 980 V to 1060 V were applied to the H8500 MA-PMTs to match the 511 keV peak position in energy spectra.

The reference detector is consists of  $4 \times 4 \times 10 \text{ mm}^3$  LYSO scintillation crystal and Hamamatsu R9800 PMT with single timing resolution of 199.9 ps [31], and it was also used to for coincidence trigger and resolving coincidence timing resolution with multiplexed block detectors.

## 2. Bipolar multiplexing circuit

Modern data acquisition system uses analog-digital convertors (ADCs) which are capable of determining polarity of pulse signals, however PET detectors only give out single polarity pulsed signal and uses only half of ADC's dynamic range, which is not efficient. The proposed multiplexing circuit (bipolar multiplexing) multiplexes block detectors by encoding the position related signal outputs with different combination of polarity (Table 2- 1), it is possible to distinguish the detectors with shared readout channel (Figure 2- 2)

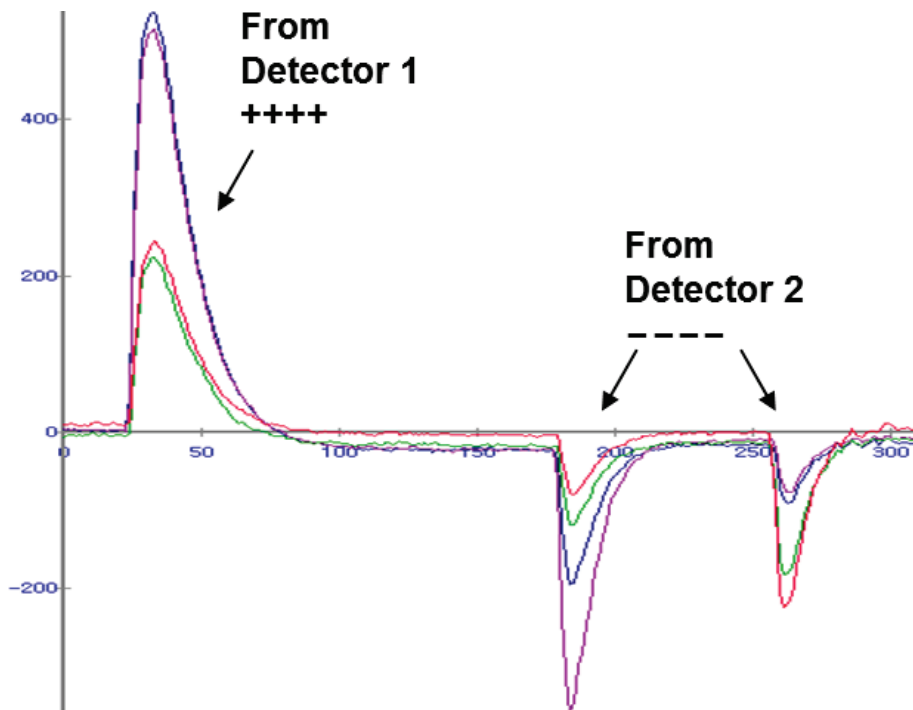


Figure 2- 2 Sampled pulses of multiplexed position related signals

The bipolar multiplexing circuit consists of 4 difference amplifiers and one summing amplifier. Four position related signals (A, B, C and D) from block detector are connected to the difference amplifiers with different combination (Table 2- 1) of positive or negative signal inputs. Dynode signals connected to summing amplifier (Figure 2- 3 and Figure 2- 4). Various multiplexing ratios of 1:1, 2:1, 4:1, 8:1 and 16:1 are supported with the proposed multiplexing circuit without additional components. The gain of amplifiers in the multiplexing circuit decreases as the number of connected block detector increases, since the output impedance of block detector outputs makes parallel connection. Therefore, the gain of amplifiers is adjusted for different multiplexing ratio to match energy peak (511 keV) position.

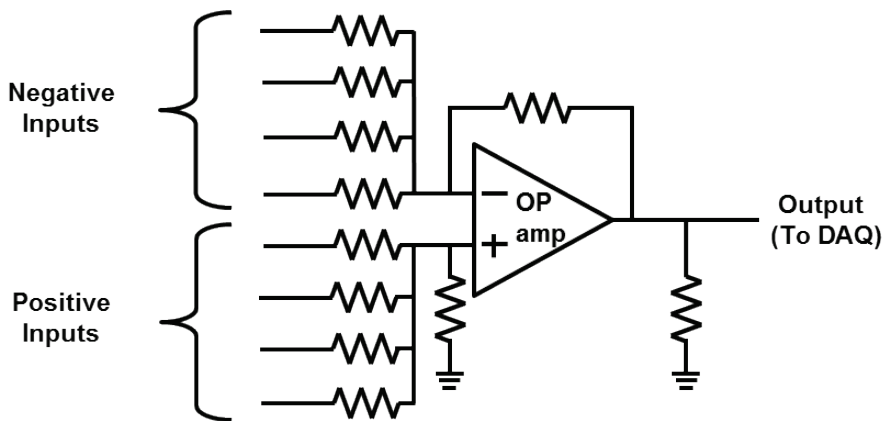


Figure 2- 3 Circuit configuration for difference amplifier used in multiplexing.

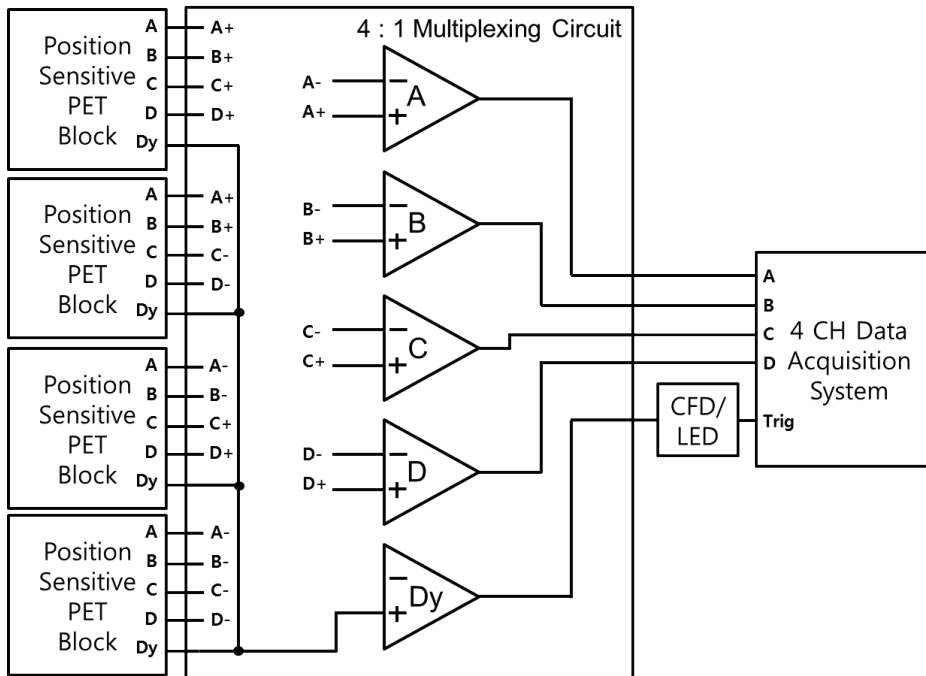


Figure 2- 4 Example of 4:1 multiplexing circuit

Detector ID	Polarity of signals (A, B, C, D)				
	1:1	2:1	4:1	8:1	16:1
1	++++	++++	++++	++++	++++
2		----	++--	++--	+++-
3			---+	+-+-	+-+-
4			----	+---	+---
5				-+-+	-+-+
6				-+-+	-+-+
7				---+	---+
8				----	+---
9					-+++
10					-++-
11					-+-+
12					-+--
13					--++
14					--+-
15					----+
16					----

Table 2- 1 Polarity combination table for bipolar multiplexing

### 3. Data acquisition setup

Data were acquired by using coincidence trigger of multiplexed block detectors and the reference detector. Constant-fraction discriminators (CFD, output width of 20 ns, threshold of 10 mV: CAEN N842, Italy) are used to generate trigger signals from dynode signals and a coincidence trigger signal is generated with logic AND unit (CAEN N455, Italy). Analog signals from the multiplexing circuit, 4 position related signals and a dynode signal, and a dynode signal from the reference detector are sampled with domino ring sampling 5GS/s digitizer (DT5742; CAEN S.p.A., Italy) (Figure 2- 5). The signals are acquired by the coincidence trigger, which is connected to fast trigger port of the digitizer. For every coincidence trigger input, 1024 samples (total duration: 204.8 ns) of all signals are acquired and transferred to computer via USB. Count rates of multiplexed block detectors were measured with a NIM counter (CAEN N1145, Italy).

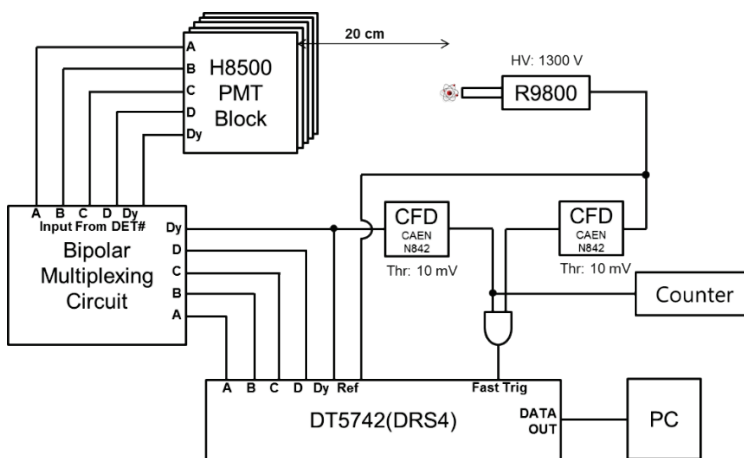


Figure 2- 5 Block diagram showing the experimental setup to acquire coincidence data with DRS4 based data acquisition system

#### 4. Generation of flood histogram

Five hundred out of 1024 samples (100 ns integration) of each position-related signal were integrated to obtain the energy, position and polarity information of the signals. The baseline was corrected by averaging 100 samples (20 ns) prior to the pulse. The block detectors were identified by the polarity of the position-related signal. The position (X, Y) and the energy (E) of each event was calculated with the following formulas.

$$\begin{aligned} X &= \frac{(|A|-|D|) + (|B|-|C|)}{|A|+|B| + |C|+|D|} \\ Y &= \frac{(|A|-|B|) + (|D|-|C|)}{|A|+|B| + |C|+|D|} \\ E &= |A| + |B| + |C| + |D| \end{aligned} \tag{1}$$

## **5. Timestamp extraction**

Timestamp of each event is extracted from sampled dynode signals using digitally calculated CFD. The initial timestamp supplied at a resolution of 200 ps, which corresponds to data sampling rate of digitizer, is not sufficiently fine for analyzing timing resolution. The sampled dynode signal was interpolated with factor of 20 using linear interpolation to find the crossing time of constant-fraction of the peak value of the pulse with higher accuracy.

## 6. Performance evaluation

The performance of the multiplexed block detectors was evaluated for 1:1, 2:1, 4:1, 8:1 and 16:1 multiplexing ratios at different count rates. Different count rates were yielded by changing the distance between the block detectors and a  $^{68}\text{Ge}$  source placed outside coincidence detection area. The parameters used to evaluate the changes due to the application of signal multiplexing were the quality of flood histogram, the energy resolution and the coincidence resolving time (CRT). To quantify the flood histogram degradation caused by multiplexing and different count rates, flood histogram quality parameter  $k$  was calculated on all crystal peaks ( $m \times n$ ) in the flood histogram as follows:

$$k = \frac{1}{2} \left( \frac{1}{(n-1)m} \sum_{j=1}^m \sum_{i=1}^{n-1} \frac{x_{(i+1)j} - x_{ij}}{(w_{x(i+1)j} + w_{xij})/2} + \frac{1}{(m-1)n} \sum_{i=1}^n \sum_{j=1}^{m-1} \frac{y_{i(j+1)} - y_{ij}}{(w_{yi(j+1)} + w_{yij})/2} \right) \quad (2)$$

Where  $w_{xij}$  and  $w_{yij}$  are the full widths at half maximum (FWHM) of the Gaussian fitted  $x$  and  $y$  projections of flood histogram of crystal at  $(i, j)$  position,  $x_{ij}$  and  $y_{ij}$  are the centroids of the flood histogram of crystal at  $(i, j)$  position. The parameter  $k$  corresponds to the average ratio of the width of the crystal measured in the flood histogram and the separation distance between neighboring crystal peaks in the  $x$  and  $y$  directions. Larger values of  $k$  correspond to better quality of flood histogram, since the crystals are separated farther. The parameter  $k$  higher than 1.00 and 2.00 corresponds to separation of individual crystals with error of 12% and 0.93% respectively.

The energy resolution was calculated for all crystal positions, and the CRT

was calculated using the time difference distribution between timestamps for coincidence events of 410–610 keV in the energy distribution. The average energy and CRT of all crystals were used for evaluations.

## 7. Experiment

Coincidence data was acquired with coincidence of a multiplexed detector and a reference detector with distance of 20 cm. A  $^{22}\text{Na}$  point source with a nominal diameter of 0.25 mm was placed on reference detector's center of front surface (Figure 2- 5). We acquired 1.1 M valid events to explore the performance for all multiplexing ratios (1:1, 2:1, 4:1, 8:1 and 16:1) at different count rates and evaluated one of typical detectors. For the verification of peak separation on flood histograms in the 16:1 multiplexing condition, 16 block detectors were arranged in a circle and two  $^{22}\text{Na}$  point sources were placed around the center of circle to evenly irradiate the block detectors. For every block detectors, 0.5 M events were acquired in single-acquisition mode at total count rate of 320 kcps from all block detectors.

## RESULTS

Figure 2- 6 shows the experimental results obtained using the proposed multiplexing method with all multiplexing ratios (1:1, 2:1, 4:1, 8:1 and 16:1) at different count rates. Figure 6 (a) shows the changes in energy resolution at different multiplexing ratios and count rates. There is no significant degradation due to multiplexing, but the degradation is seen as total count rate of all blocks increases. This result demonstrates that signal multiplexing is not a main factor of energy resolution degradation.

The CRT (Figure 2- 6 (b)) shows that degradation increases as the count rate of multiplexed block detector increased. This means that the CRT performance is determined by multiplexing ratio as well as by the count rate. Front-end circuit and photo-sensor noise are accumulated by multiplexing block detectors, causing the degradation in timing performance. The flood histogram parameter  $k$  (Figure 2- 6 (c)) shows that degradation increases as the ratio of multiplexing and count rate increased.

Figure 2- 7 shows the flood histograms of a block detector and the line profile of the 14<sup>th</sup> row at two average count rate ranges (6-8 kcps and 70-90 kcps per block detector). As the multiplexing ratio is increased, the quality of the flood histogram and the line profile is degraded and the degradation is greater at higher count rate. All the flood histograms in the 16:1 multiplexing conditions were well de-multiplexed as shown in Figure 2- 8.

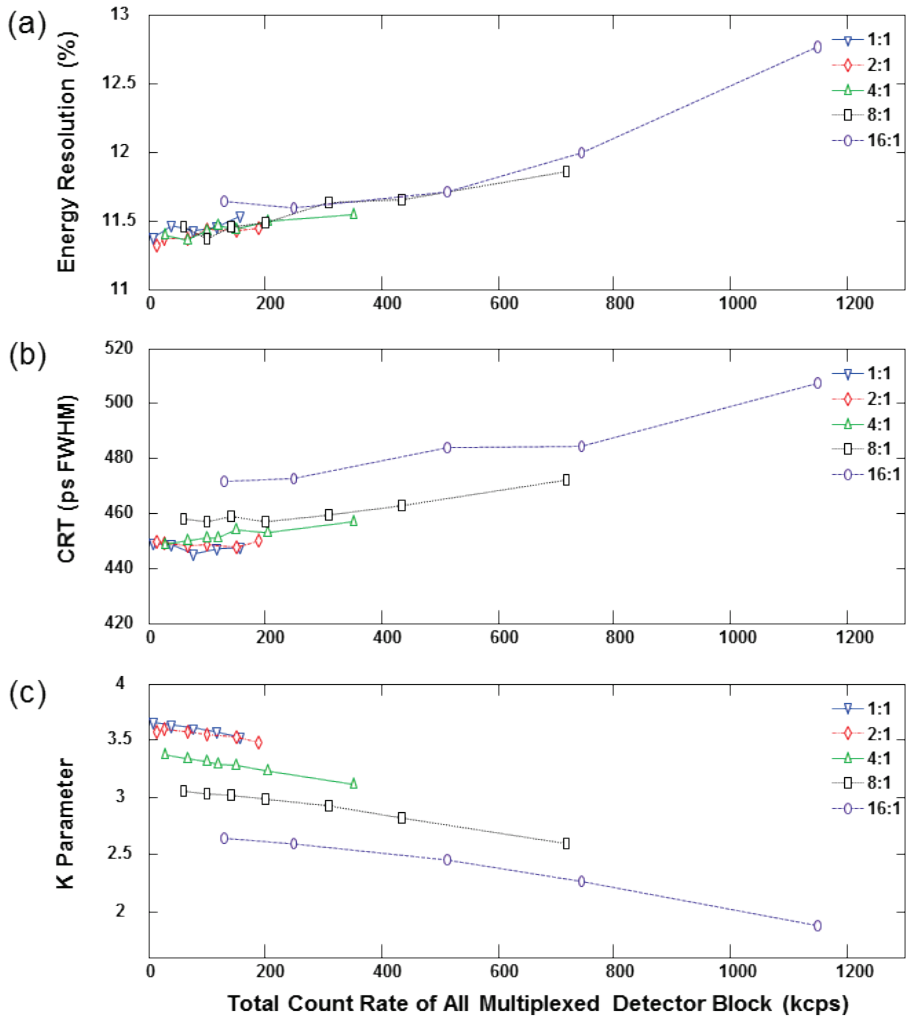


Figure 2- 6 Changes in global average energy resolution (a), global average coincidence resolving time (CRT) (b) and flood histogram quality parameter  $k$  (c) of two block detectors in various multiplexing ratios

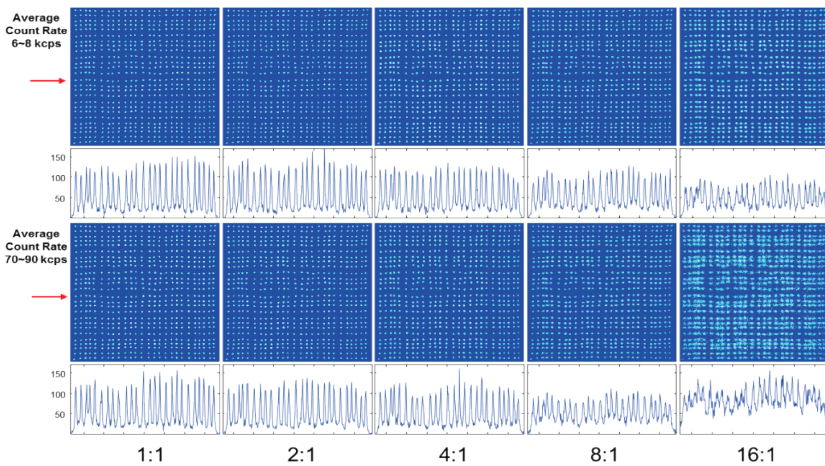


Figure 2- 7 Flood histograms and line profile of two block detectors for all multiplexing ratios

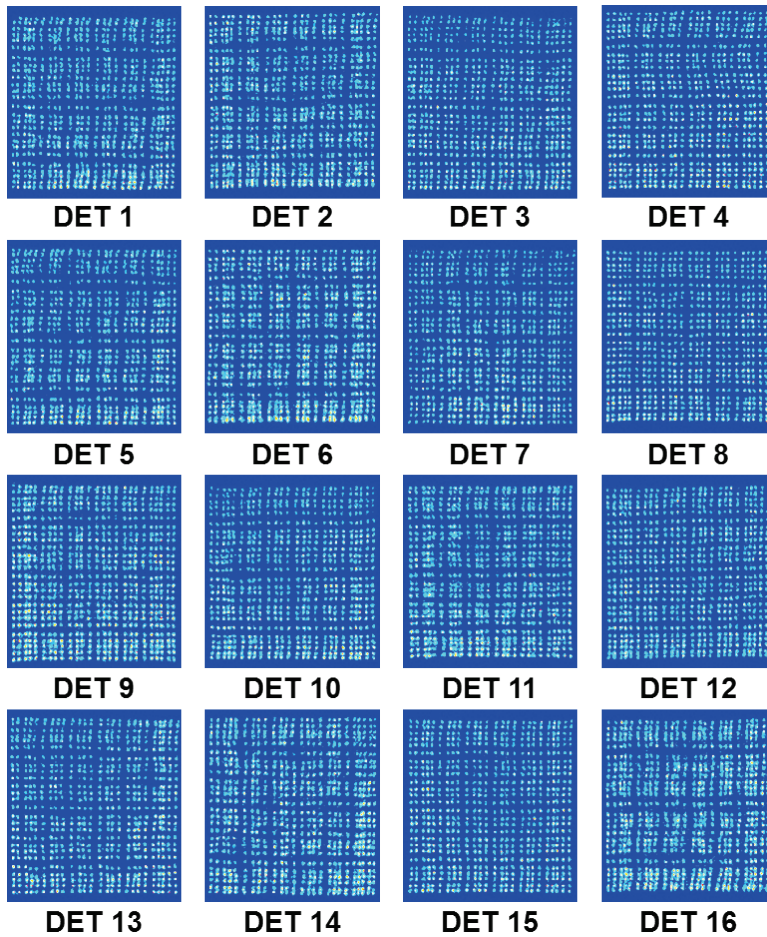


Figure 2- 8 Flood histograms of 16 block detectors multiplexed with 16:1 bipolar multiplexing circuit

# DISCUSSION

## 1. Advantages of bipolar multiplexing

Multiplexing of block detectors before the digitization reduces the required number of readout channel by multiplexing ratio, decreasing system cost and power. Multiplexing technique also reduces the number of signal transmission lines. Without multiplexing, each block detector requires 5 signal lines (4 position sensitive + 1 common). On the other hand, for the example with the 16:1 multiplexing method, 16 detector modules only require 5 signal lines, a 93.75% reduction in signal transmission lines without changes in data acquisition system. This method gives out almost equivalent flood histogram as non-multiplexed block detector. The flood histograms acquired by the multiplexing method did not require any changes in subsequent processing for crystal identification compared to the non-multiplexed ones.

When this multiplexing method is applied to the systems using differential signal transmission for analog signal readout, polarity of signals can be inverted simply by reversing the polarity of transmitter output against receiver input (Figure 2- 9).

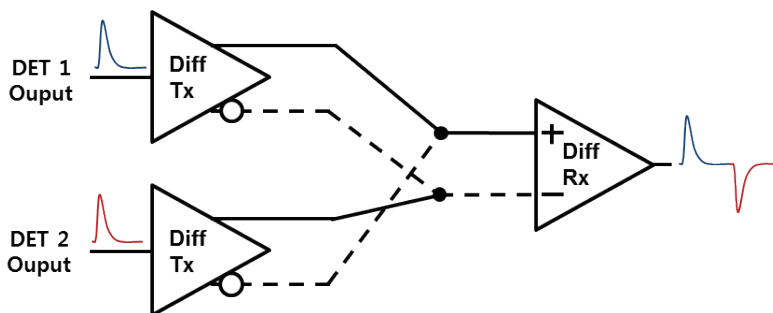


Figure 2- 9 Multiplexing method with differential signaling

The proposed bipolar multiplexing method in this work is applied to prototype MA-PMT based PET scanners under development in our group with different multiplexing ratios (2:1 and 4:1). With this multiplexing method, 50% ~ 75% of reduction in wire routing and readout channels was possible depending on multiplexing ratio. The bipolar multiplexing is not only dedicated for MA-PMT based position sensitive block detectors, it is also possible to use for all position sensitive detectors that give out single polarity pulse. The bipolar multiplexing method was also successfully applied to SiPM based PET inserts for simultaneous PET/MR imaging with multiplexing ratio of 2:1 and 8:1 [32, 33].

## **2. Limitation of bipolar multiplexing**

The number of block detectors that can be multiplexed (ratio of multiplexing) is limited by the gain and noise of the system. The noise of the system increases as the number of multiplexed detectors increases, resulting in degradations of system performance such as flood histogram quality and timing resolution (Figure 2- 6). The source of noise are intrinsic activity and after pulse of the scintillation crystal, thermally induced noise of photo-sensors (dark current for PMTs or dark count for SiPM) and electrical noise caused by front electronics such as preamplifiers. As aforementioned noise sources are proportional to the area of detector face, the maximum number of block detectors that can be multiplexed is mainly determined by the total area of multiplexed detectors. Additionally, with photo-sensor that produces pulse like noise such as SiPM (produces dark counts), the SNR of flood images decrease as the area of photo-sensors increases. The multiplexing of block detectors that use such photo-sensors will decrease the SNR of flood images even more compared to the ones with less noisy photo-sensors such as PMT.

Another factor that limits the number of detectors that can be multiplexed is the required count rate performance for each block detectors. As the multiplexed block detectors share the readout channels, required count rate performance for each channel is the sum of count rates for each block detectors. Probability of pulse pile-up increases as multiplexing ratio increases at same count rate per block detector, causing performance degradation in energy resolution, CRT and flood histogram quality as shown in Figure 2- 6. Therefore, the ratio of multiplexing must be determined by the required count rate per

block detector and the maximum count rate performance of readout channel.

However, there are several methods to improve count rate performance of readout channel. One of them is to implement pulse pile-up correction [12] into data acquisition system, which would recover overlapped pulses and increase count rates limits per channel. Another possible approach to improve count rate performance of multiplexed system would be to implement analog filtering circuit to reduce the width of pulse [11]. As the probability of pulse pileup overlap is proportional with count rate and pulse width, the reduction of pulse width will lead to less probability of pulse pileup, therefore higher count rate can be achieved.

## CONCLUSIONS

A bipolar analog multiplexing method was developed for position sensitive block detector based PET system that requires high sensitivity. It is verified through experiment that the multiplexing of block detectors did not significantly degrade timing, energy and spatial performance while reducing required number of data acquisition channels and wire routing density. The method described and test in this study will be useful for not only for PET systems, but also for other NM imaging systems (gamma cameras, SPECT) that uses position sensitive block detectors.

# **CHAPTER 3**

## **Application to the PET System for Simultaneous PET-MRI Imaging**

# INTRODUCTION

A hybrid positron emission tomography/magnetic resonance imaging (PET/MRI) scanner has many potential advantages, including a reduced radiation dose, better soft tissue contrast on MRI than X-ray computed tomography (CT), almost unlimited combination of functional and molecular information, and possible motion correction of the PET image using MR data [34–37]. However, simultaneous PET/MR imaging with a conventional photomultiplier tube (PMT)-based PET camera is technically challenging, because the PMT is highly sensitive to the magnetic field. Almost every property of the PMT PET signal is distorted within the magnetic field. For example, the energy spectrum of the PET detector is quite shrunken because of the loss of PMT signal output, and the peak position of the scintillation crystal cannot be distinguished in the flood maps of block detectors [34]. Therefore, if relatively long optical fiber bundles are not used, the PMT PET camera should be placed a distance from the MRI machine [38]. Consequently, a longer scan time is required, patient throughput is low, and the chance of patient movement increases with this type of PET/MRI scanner.

In contrast, semiconductor photo sensors are not susceptible to electromagnetic interference because the electrical signal pathways in these devices are much shorter than in the PMT. The most-investigated semiconductor photo sensor for MR-compatible PET detectors is the avalanche photodiode (APD). The feasibility of APD PET inserts for small animal and human brain PET/MRI studies have been shown by several groups [39–42], and

the first commercial APD PET/MRI scanner for whole-body imaging has recently been introduced.

Although the APD PET detector is a mature technology, it has known limitations, including a lower gain of signal amplification and inferior timing resolution compared to PMT. Alternatively, the silicon photomultiplier (SiPM)—also called a Geiger-mode APD (G-APD), solid-state photomultiplier (SSPM), multipixel photon counter (MPPC)—is gaining much attention as a promising photo sensor for future PET/MRI systems, because it is insensitive to the magnetic field and has amplification gain and timing resolution equivalent to that of the PMT [43–45]. Therefore, several groups, including us, have worked on the development of SiPM PET detectors and systems [46–52].

Recently, we have shown the feasibility of our first SiPM PET prototype for small animal imaging [51]. The first prototype system consisted of eight SiPM detector modules composed of  $4 \times 13$  LGSO ( $\text{Lu}_{1.8}\text{Gd}_{0.2}\text{SiO}_4:\text{Ce}$ ) crystals and  $2 \times 6$  SiPMs, and it had a ring diameter of 6.0 cm and an axial field of view (FOV) of 0.65 cm. Although this system showed excellent 1.0-mm spatial resolution, its sensitivity ( $<0.1\%$ ) and energy resolution (26%) were not good enough for routine animal imaging studies. Therefore, we have worked on the second version of the SiPM PET system to improve the performance of SiPM PET, which enables simultaneous PET/MR image acquisition. In this second scanner, we are using a multichannel MPPC (Hamamatsu Photonics, Hamamatsu, Japan) to extend the ring diameter and the axial FOV to 13.6 and 3.2 cm, respectively.

We describe here the MR-compatible SiPM PET scanner and present initial

results of simultaneous PET/MRI experiments on phantom and living animal to demonstrate the feasibility of our new system.

# MATERIALS AND METHODS

## 1. PET Detector Module

The scintillation crystal used in the PET detector module was LGSO ( $\text{Lu}_{1.8}\text{Gd}_{0.2}\text{SiO}_4: \text{Ce}$ ) (Hitachi Chemical, Ibaraki, Japan). We choose LGSO because it has a fast scintillation decay time ( $\tau = 41 \text{ ns}$ ), good stopping power ( $\mu = 0.85 \text{ cm}^{-1}$  at 511 keV), and high light output. It has yielded outstanding performances in our previous investigations [10, 51], and its MR compatibility was confirmed [53]. The LGSO array consists of 360 ( $20 \times 18$ ) crystals (Figure 3- 1), each measuring  $1.5 \times 1.5 \times 7.0 \text{ mm}^3$ . A grid of 3M (St. Paul, MN, USA) enhanced spectral reflector (ESR) polymer with 0.065 mm thickness was used to construct the crystal array and optically isolate each of the crystals, yielding a crystal pitch of 1.62 mm.

The SiPM used in this study was the MPPC array with  $4 \times 4$  channels (S11064-050P; Hamamatsu Photonics, Hamamatsu, Japan) made up of individual SiPM chips with  $3 \times 3 \text{ mm}^2$  active areas and mounted at high densities on SMD packages. The specifications of S11064-050P are summarized in Table 3- 1. We choose the S11064-050P because it has an appropriate spectral response and number of pixels per channel in combination with LGSO crystals. For each detector module, four S11064-050Ps were combined to yield  $8 \times 8$  SiPM channels, as shown in Figure 3- 1. Four S11064-050Ps for each module were carefully selected to yield the minimal variability in optimal operating bias voltages (bias voltage to yield an amplification gain of  $7.5 \times 10^5$ ) across the 64 SiPM channels. Thus, the standard deviation of

optimal bias voltage for SiPM was  $<0.03$  V in all detector modules.

Soft polyvinyl chloride (PVC) with 1.0 mm thickness was inserted between the  $20 \times 18$  LGSO and  $8 \times 8$  SiPM arrays for light spreading. Optical grease with a refractive index of 1.46 was then applied to the interface between them.

Parameter	Value
No. of channels	16 ( $4 \times 4$ )
Effective area per channel (mm)	$3 \times 3$
No. of pixels per channel	3,600
Pixel size ( $\mu\text{m}$ )	$50 \times 50$
Fill factor (%)	61.5
Peak wavelength (nm)	440
Typical gain	$7.5 \times 10^5$

Table 3- 1 Specification of SiPM (MPPC S11064-050P)

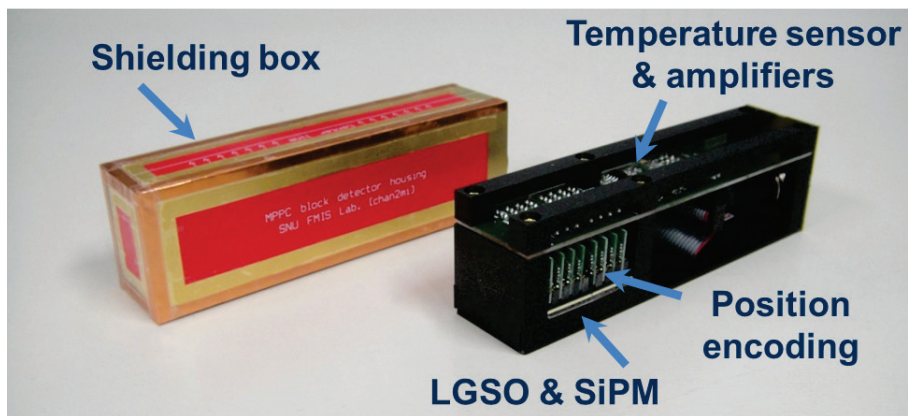


Figure 3- 1 SiPM detector module and shielding box.

## 2. Front-end Electronics

An average optimal bias voltage of 64 SiPMs was applied to each detector module. The  $8 \times 8$  SiPM output channels were connected to the position encoding circuit that consisted of a RCN and differential amplifiers (Figure 3-1). Because, we directly connected the SiPM chips to the RCN without the use of a preamplifier to make the detector module as compact as possible, each SiPM channel has a different input impedance. Therefore, the resistor values of the charge division circuit were determined to match the input impedance from each SiPM channel using PSpice software for simulation of SiPM and RCN.

For continuous monitoring of the temperature change in the detector module, a solid-state temperature sensor (TCN75; Microchip Technology) with a temperature accuracy of  $0.5^{\circ}\text{C}$  was added to the printed circuit board (PCB). A dedicated temperature monitoring program developed previously [51] was used to collect the temperature data via serial interface with TCN75 and record it every second.

### 3. MR-Compatible PET Scanner

Each of the detector modules was enclosed in a copper shielding box (thickness of the copper was 18  $\mu\text{m}$ ) to block the interference between the PET and MRI systems. We adopted a modular design to minimize the induction of eddy currents around the shielding box (Figure 3- 1). As shown in Figure 3- 2, a total of 12 detector modules were arranged in a ring shape with 13.6 cm distance between the front surfaces of the opposite detector modules (Table 3- 2).

We used nonmagnetic shielded-twisted-pair (FTP) cables to transfer the output of the differential amplifiers to the data acquisition system located outside the MR room to minimize any interference by radiofrequency (RF) signals. To isolate the shielding ground, the isolation panel was used to route signals from inside the MR room to outside it.

<b>Parameter</b>	<b>Value</b>
No. of channels	<b>16 (4 × 4)</b>
Effective area per channel (mm)	<b>3 × 3</b>
No. of pixels per channel	<b>3,600</b>
Pixel size ( $\mu\text{m}$ )	<b>50 × 50</b>
Fill factor (%)	<b>61.5</b>
Peak wavelength (nm)	<b>440</b>
Typical gain	<b><math>7.5 \times 10^5</math></b>

Table 3- 2 Major characteristics of MRI-compatible SiPM PET

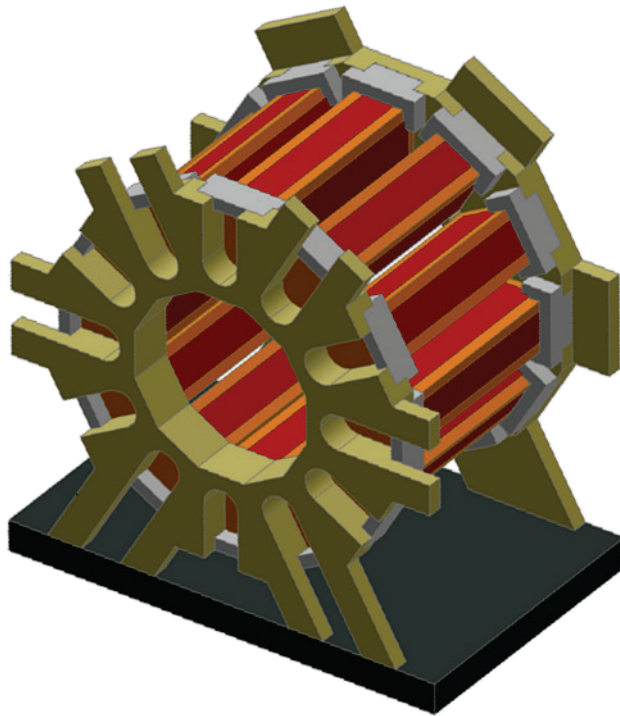


Figure 3- 2 MRI-compatible SiPM PET scanner consisting of 12 detector modules

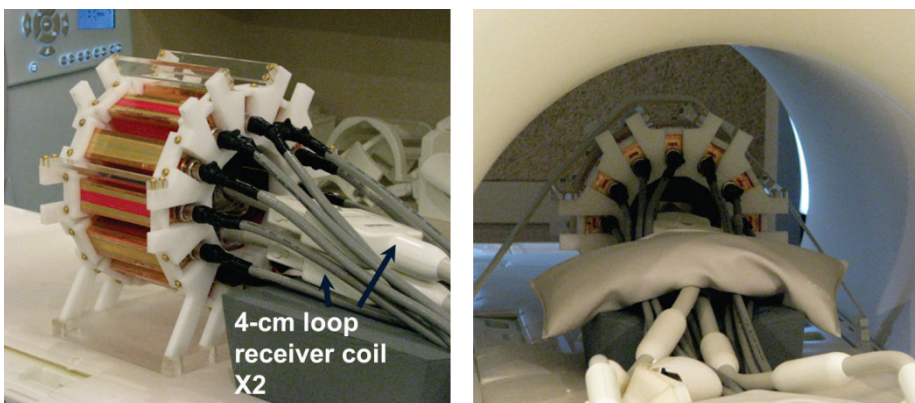


Figure 3- 3 SiPM PET insert placed outside and inside 3-T MRI scanner Simultaneous PET/MR Imaging

## **4. PET Performance Evaluation**

We conducted a preliminary performance evaluation of the PET system. Energy resolution of a detector block was measured using a  $^{22}\text{Na}$  point source. In addition, spatial resolution and sensitivity at the center of the FOV were evaluated by following the National Electrical Manufacturers Association (NEMA) NU4-2008 protocols [54].

## 5. MR Compatibility Tests

The MR compatibility tests and simultaneous PET/MR image acquisitions were performed inside a 3-tesla (T) clinical MRI system (MAGNETOM Trio; Siemens) with 4-cm loop receiver coils located inside the PET system. MR RF waves were transmitted from the main body coil. A custom-made coil holder and animal bed were used for reproducible positioning of the RF coil, to prevent the motion artifact due to coil vibration, and for mouse and rat imaging studies (Figure 3- 3). To explore whether the magnetic field and RF signals influenced the quality of the PET data, we obtained PET flood histograms and energy histograms with the PET insert placed inside the magnet, with and without the MR sequence, as well as outside the magnet (Figure 3- 3).

The MR images of a set of cylindrical phantoms filled with water were acquired with and without the PET insert inside the magnet to evaluate the effect of the PET insert on MR images. In addition, images were acquired with the PET insert powered on and off to determine the effect of PET electronics.

To demonstrate the feasibility of simultaneous PET/MR images with this system, sets of PET and MR images were acquired simultaneously using the SiPM PET insert and two loop receiver coils. We acquired PET/MR images of  $^{18}\text{F}$ -filled capillary tubes (inner diameter 1.1 mm; activity 6.5 MBq) inserted in a cucumber to mimic the living animal studies for 40 min. The capillary tubes were placed along the axis of the scanners, and MR images were acquired using a standard T2 turbo spin echo (TSE) sequence (TR/TE 8000/107; matrix size  $384 \times 384$ ; slice thickness 0.8 mm).

Mouse study was approved by the Institutional Animal Care and Use

Committee at Seoul National University. During the PET experiments, 25-g BALB/c mouse was anesthetized by continuous administration of isoflurane in oxygen.  $^{18}\text{F}$ -FDG (3.7 MBq) was injected through the tail vein, and 30 min later a 60-min image data set was acquired. T2 TSE MR images were acquired during the PET scan.

## 6. Data Processing

For normalization correction, scans were acquired using an annulus phantom (inner diameter 69 mm; thickness 2 mm) filled with  $^{68}\text{Ga}/^{68}\text{Ge}$  covering the entire FOV. Different source thicknesses were compensated for each line of response (LOR) in the normalization data. The list-mode data set was sorted into a three-dimensional sonogram, and then rebinned into two-dimensional data using the single slice rebinning (SSRB) method.

All scanned PET data were reconstructed using maximum likelihood expectation maximization (MLEM) reconstruction with exact position information for each LOR element. An isotropic Gaussian filter with a 0.5-mm full width at half-maximum (FWHM) was applied to the reconstructed images. The image fusion of PET and MRI was performed using software for functional image registration (FIRE; Seoul National University) [55].

# RESULTS

## 1. Physical Performance of SiPM PET

The energy resolution for an individual crystal in a typical detector block was about 13.9%, which has been much improved from the first prototype (~26%). The photopeak region was clearly separated from the scattered events in the energy spectrum of each crystal.

Radial and tangential spatial resolutions at the center of the FOV were 1.0 and 1.2 mm, respectively, which are similar to those obtained from the first prototype. Sensitivity at the center was 0.195% with an energy window of 250–750 keV, which is 2.3 times higher than the first prototype.

## **2. Interference between PET and MRI**

Raw PET signals recorded using a 350-MHz oscilloscope (MSO 4034; Tetronix, Beaverton, OR, USA) from the SiPM PET insert located inside the MR magnet while running various RF sequences showed no difference from those acquired outside the MR room. In addition, the RF sequences did not lead to any change in the flood map (Figure 3- 4) or the global energy spectrum of SiPM PET detector modules.

On the other hand, MR phantom images acquired with the PET insert (power on) located inside the magnet showed no obvious artifacts except for a slight degradation of image quality in comparison to the one without the PET insert (Figure 3- 5). The MR image quality was not changed by turning off all power supplies to the PET insert, indicating that the image quality degradation is not caused by electromagnetic interference from the PET electronics. The main reason is likely partial obstruction of RF waves from the main body coil by the PET insert.

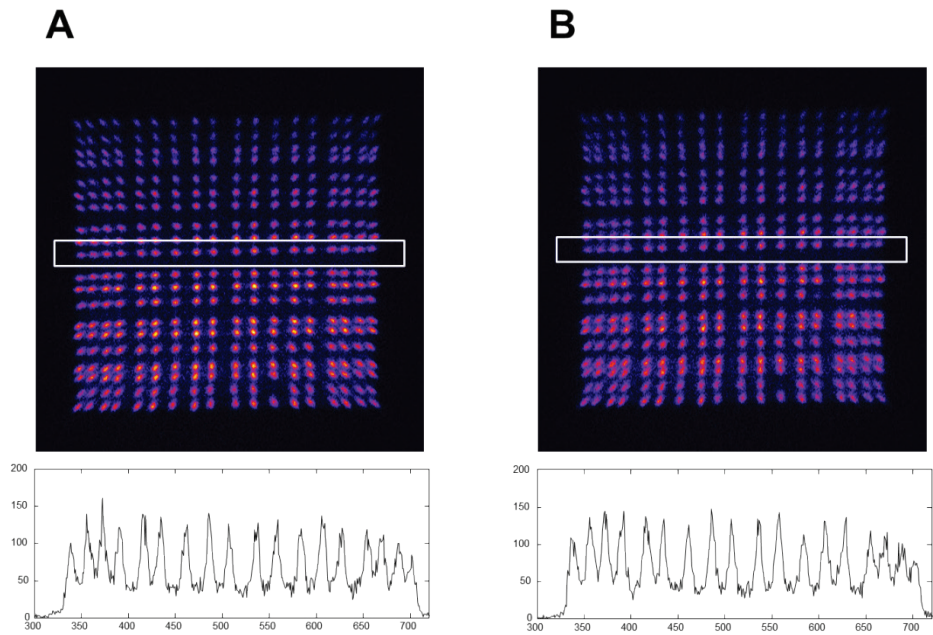


Figure 3- 4 Flood histograms of SiPM PET detector module acquired without (A) and with (B) application of radiofrequency pulse sequences, and profiles on them. Boxed regions are where profiles were estimated

Parameter	Without radiofrequency	With radiofrequency
Mean	<b>3.50</b>	<b>3.49</b>
SD	<b>0.97</b>	<b>1.03</b>

Table 3- 3 Peak-to-valley ratio along profiles on middle rows in flood histograms shown in Figure 3- 4

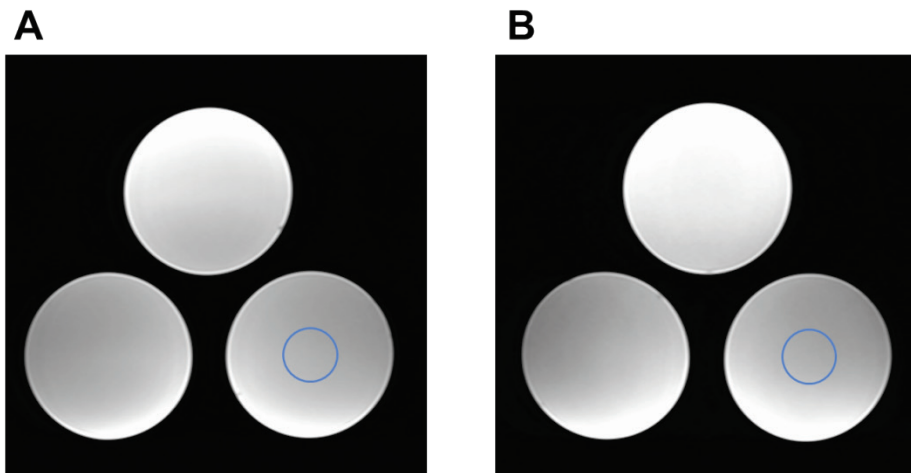


Figure 3- 5 T2-weighted MRI scans of uniform cylindrical phantom acquired without (A) SiPM-PET insert and with (B) insert (power on). Circled regions are where signal-to-noise ratio, summarized in Table 3- 4, was estimated

<b>Parameter</b>	<b>Without PET</b>	<b>With PET</b>
Intensity	<b>3.50</b>	<b>3.49</b>
Signal-to-noise- ratio	<b>0.97</b>	<b>1.03</b>

Table 3- 4 Summary of average signal intensity and signal-to-noise ratio of MRI scans shown in Figure 3- 5

### 3. Simultaneous PET/MR imaging

Figure 3- 6 and 3- 7 show the first simultaneous PET and MR images of a cucumber phantom and living mouse using the present system. The  $^{18}\text{F}$ -PET and T2 MRI images of capillary tubes inserted into the cucumber show good spatial resolution of both imaging systems and accurate geometrical alignment of both images with minimal spatial nonlinearities (Figure 3- 6).

Figure 3- 7 shows the PET and T2 MR images of a BALB/c mouse acquired 30 min after injection of  $^{18}\text{F}$ -FDG. Note that transverse slices in the kidney level are shown, and both kidneys are well visualized without any distortion of images or local mismatches.

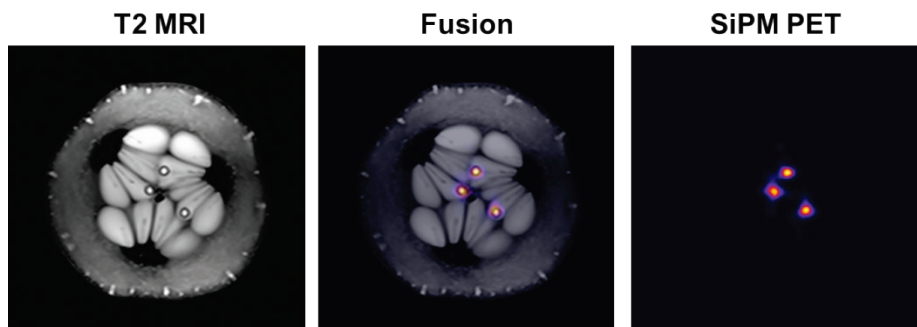


Figure 3- 6 Simultaneously acquired PET and MRI (T2-weighted turbo spin echo) scans of three  $^{18}\text{F}$ -filled capillary tubes inserted into cucumber.

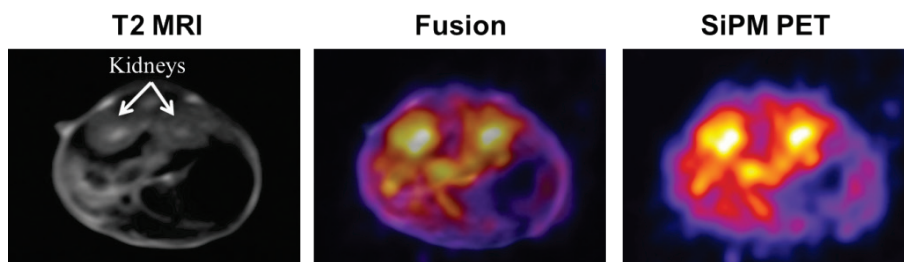


Figure 3- 7 In vivo PET/MRI (T2-weighted turbo spin echo) study in BALB/c mouse after injection of  $^{18}\text{F}$ -FDG

## DISCUSSION

We developed an MR-compatible SiPM-based PET scanner and combined this scanner with a state-of-the-art 3-T MRI system. We also showed the feasibility of this combined system by performing various simultaneous PET/MR imaging studies.

As mentioned previously, there are several advantages of SiPM over APD as a semiconductor photo sensor in an integrated PET/MRI system. In particular, the higher gain of signal amplification due to the operation in Geiger mode is an advantageous property of SiPM for reducing the complexity of front-end electronics for analog signal readout from the photo sensors. Being different from the APD-based small animal PET/MRI systems that employ application-specific integrated circuits (ASIC) chips for individually coupling each APD channel to a preamplifier [40, 41], we directly connected SiPM channels to the RCN circuit without the use of preamplifiers.

Because of the much-reduced dark count rate in the state-of-the-art SiPM (S11064-050P;  $\sim 6$  Mcps) the incorporation of 64 SiPM channels in a single RCN circuit and application of a wider signal integration time window of 200 ns for analog-to-digital conversion were possible in this study, whereas our previous system [51] had 6 channels in an RCN and a 20-ns integration window. These differences contributed to the extension of the axial FOV and improvement in energy resolution, respectively. The multiplexing signals using the RCN circuit to reduce the number of output channels from the PET detectors was also useful for simplifying wire routing and effectively shielding the wires,

in contrast to other approaches using wire bundles [56, 57] for 1-to-1 coupling of SiPM with a preamplifier.

The fluctuation in SiPM gain with regard to the operating bias voltage is an important technical issue in SiPM-based PET detector development [43, 44]. Moreover, each SiPM chip has a different operating voltage level to produce the same gain of signal amplification. This is why we combined four S11064-050Ps with a minimum difference in the average optimal operating voltage in each detector module. Although we applied the same bias voltage to 64 SiPM channels in four S11064-050Ps to minimize the number of power lines, the flood maps showed a uniform count distribution, as shown in Fig. 4, commonly with or without RF application.

The gain of SiPM is also dependent on temperature [43, 44, 58]. The temperature-dependent gain variation of MPPC is  $\sim 5\%$  per degree at room temperature [50, 59]. In this study, used the gain compensation method in which the ADC output is scaled retrospectively using the temperature information measured continuously during PET/MRI data acquisition. Because of the well-maintained temperature at about  $20^{\circ}\text{C}$  in the MRI scanning room, the retrospective gain compensation method was a practical solution in our preliminary phantom and animal studies. However, we may need more investigation into the feasibility of this compensation method when we incorporate a heated animal stage to maintain the body temperature of animals. Because other physical properties of SiPM (i.e., the dark count [noise] rate) are also negatively influenced by increasing the temperature, more active temperature insulation of PET detector modules would be useful. The tradeoff

between performance and complexity should be considered in future studies.

Radiofrequency waves induce the electric current inside the conductive material, incurring noise in the PET readout electronics [43]. In previous studies, we also reported radiofrequency-induced events in the PET electronics that matched radiofrequency pulses [43, 47]. In contrast, there was no noise from the radiofrequency in this PET system. In this study, we optimized the shielding method and used several techniques to avoid radiofrequency noise. The techniques included the use of nonmagnetic foil-screened twisted-pair cables to transfer the output of the differential amplifiers and isolation panel so as to route signals from inside the MRI room to outside it and isolate the shielding ground. The conductive shielding materials of the foil-screened twisted-pair cables and the isolation panel form a faraday cage that isolates the signal path from the environment with its radiofrequency noise. Therefore, induction of radiofrequency noise to signal lines is avoided.

Although small animal-dedicated ultra-high-field (i.e., 9.4T or 7.0T) MRI scanners yield better spatial resolution and image quality, the combination of a SiPM PET scanner with a widely used clinical 3.0-T or 1.5-T MRI system would also have a rationale. In particular, the much higher availability of advanced pulse sequences and techniques in clinical 3.0-T and 1.5-T systems is one of them. In some translational research from animal experiments to human applications (e.g., development of contrast agents), the clinical system would be preferred rather than ultra-high-field systems. More available space inside the MR bore than is allowed in dedicated animal MRI scanners is another merit of the clinical MRI system. The larger space allows the utilization of longer

scintillation crystals and various depth-of-interaction measurement techniques to improve PET system performance [3].

In the investigation of MRI-compatible PET inserts with state-of-the-art clinical MRI systems, one practical challenge is the current MRI trend to use powerful body coils to transmit radiofrequency waves and local radiofrequency coils to receive signals. Use of dedicated local radiofrequency coils to transmit and receive radiofrequency to and from objects would be an effective way to avoid the partial obstruction of waves from the main body coil by the PET insert. Another possible approach is incorporation of short optical fiber bundles between the scintillation crystal array and SiPMs to minimize the obstruction provided by the electronics and shielding materials [39, 60].

## **CONCLUSIONS**

We developed an MR-compatible SiPM PET insert with 12 detector modules. We found that simultaneous PET/MR imaging was possible using this multichannel SiPM-based PET insert with no RF interference on PET signals or images and only slight degradation of MR scans

## REFERENCES

1. Pichler BJ, Wehrl HF, Judenhofer MS (2008) Latest advances in molecular imaging instrumentation. *J Nucl Med* 49 Suppl 2:5S–23S
2. Lewellen TK (2008) Recent developments in PET detector technology. *Phys Med Biol* 53:R287–317
3. Ito M, Hong SJ, Lee JS (2011) Positron emission tomography (PET) detectors with depth-of- interaction (DOI) capability. *Biomed Eng Lett* 1:70–81
4. Price PM, Badawi RD, Cherry SR, Jones T (2014) Ultra Staging to Unmask the Prescribing of Adjuvant Therapy in Cancer Patients: The Future Opportunity to Image Micrometastases Using Total-Body 18F-FDG PET Scanning. *J Nucl Med* 55:696–7
5. Schäfers KP (2008) The promise of nuclear medicine technology: status and future perspective of high-resolution whole-body PET. *Phys Med* 24:57–62
6. Laymon CM, Miyaoka RS, Park BK, Lewellen TK (2002) Simplified FPGA-based data acquisition system for PET. *IEEE Nucl Sci Symp Conf Rec* 2:704–707
7. Streun M, Brandenburg G, Larue H, Parl C, Ziemons K (2006) The data acquisition system of ClearPET neuro-a small animal PET scanner. *IEEE Trans Nucl Sci* 53:700–703
8. Fontaine Ré, Belanger F, Viscogliosi N, Semmaoui H, Tetrault M-A, Michaud J-B, Pepin C, Cadorette J, Lecomte R (2009) The Hardware and Signal Processing Architecture of LabPET<sup>TM</sup>, a Small Animal APD-Based Digital PET Scanner. *IEEE Trans Nucl Sci* 56:3–9
9. McElroy DP, Hoose M, Pimpl W, Spanoudaki V, Schüler T, Ziegler SI (2005) A true singles list-mode data acquisition system for a small animal PET scanner with independent crystal readout. *Phys Med Biol* 50:3323–35
10. Hong SJ, Kwon SI, Ito M, Lee GS, Sim K-S, Park KS, Rhee JT, Lee JS (2008) Concept Verification of Three-Layer DOI Detectors for Small Animal PET. *IEEE Trans Nucl Sci* 55:912–917

11. Gola A, Piemonte C, Tarolli A (2013) Analog Circuit for Timing Measurements With Large Area SiPMs Coupled to LYSO Crystals. *IEEE Trans Nucl Sci* 60:1296–1302
12. Haselman MD, Pasko J, Hauck S, Lewellen TK, Miyaoka RS (2012) FPGA-Based Pulse Pile-Up Correction With Energy and Timing Recovery. *IEEE Trans Nucl Sci* 59:1823–1830
13. Moses WW, Buckley S, Vu C, Peng Q, Pavlov N, Choong W-S, Wu J, Jackson C (2010) OpenPET: A Flexible Electronics System for Radiotracer Imaging. *IEEE Trans Nucl Sci* 57:2532–2537
14. Mann A, Grube B, Konorov I, Paul S, Schmitt L, McElroy DP, Ziegler SI (2006) A sampling ADC data acquisition system for positron emission tomography. *IEEE Trans Nucl Sci* 53:297–303
15. Newport DD, Siegel SB, Swann BK, Atkins BE, McFarland AR, Pressley DR, Lenox MW, Nutt RE (2006) QuickSilver: A Flexible, Extensible, and High-Speed Architecture for Multi-Modality Imaging. *IEEE Nucl. Sci. Symp. Med. Imaging Conf. Rec. IEEE*, pp 2333–2334
16. Kim E, Olcott P, Levin C (2010) Optical network-based PET DAQ system: One fiber optical connection. *IEEE Nucl. Sci. Symp. Med. Imaging Conf. Rec. Ieee*, pp 2020–2025
17. Pomper MG, Lee JS (2005) Small animal imaging in drug development. *Curr. Pharm. Des.* Bentham Science Publishers, pp 3247–3272
18. Green M V, Seidel J, Vaquero JJ, Jagoda E, Lee I, Eckelman WC (2001) High resolution PET, SPECT and projection imaging in small animals. *Comput Med Imaging Graph* 25:79–86
19. Tai Y-C, Laforest R (2005) Instrumentation aspects of animal PET. *Annu Rev Biomed Eng* 7:255–85
20. Conti M (2011) Focus on time-of-flight PET: the benefits of improved time resolution. *Eur J Nucl Med Mol Imaging* 38:1147–57
21. Lee JS, Kim JH (2014) Recent advances in hybrid molecular imaging systems. *Semin Musculoskelet Radiol* 18:103–22
22. Badawi RD, Kohlmyer SG, Harrison RL, Vannoy SD, Lewellen TK (2000) The effect of camera geometry on singles flux, scatter fraction and trues and randoms sensitivity for cylindrical 3D PET—a simulation study. *IEEE Trans Nucl Sci* 47:1228–1232

23. Eriksson L, Townsend D, Conti M, Eriksson M, Rothfuss H, Schmand M, Casey ME, Bendriem B (2007) An investigation of sensitivity limits in PET scanners. *Nucl Instruments Methods Phys Res Sect A Accel Spectrometers, Detect Assoc Equip* 580:836–842
24. Siegel S, Silverman RW, Cherry SR (1996) Simple charge division readouts for imaging scintillator arrays using a multi-channel PMT. *IEEE Trans Nucl Sci* 43:1634–1641
25. Popov V, Majewski S, Weisenberger AG, Wojcik R (2001) Analog readout system with charge division type output. *IEEE Nucl. Sci. Symp. Med. Imaging Conf. Rec. IEEE*, pp 1937–1940
26. Popov V, Majewski S, Welch BL (2006) A novel readout concept for multianode photomultiplier tubes with pad matrix anode layout. *Nucl Instruments Methods Phys Res Sect A Accel Spectrometers, Detect Assoc Equip* 567:319–322
27. Olcott PD, Talcott JA, Levin CS, Habte F, Foudray AMK (2005) Compact readout electronics for position sensitive photomultiplier tubes. *IEEE Trans Nucl Sci* 52:21–27
28. Lee CM, Kwon SI, Ko GB, Ito M, Yoon HS, Lee DS, Hong SJ, Lee JS (2012) A novel compensation method for the anode gain non-uniformity of multi-anode photomultiplier tubes. *Phys Med Biol* 57:191–207
29. Lau FWY, Vandenbroucke A, Reynolds PD, Olcott PD, Horowitz M a, Levin CS (2010) Analog signal multiplexing for PSAPD-based PET detectors: simulation and experimental validation. *Phys. Med. Biol.* pp 7149–74
30. Kwon SI, Hong SJ, Ito M, Yoon HS, Lee GS, Sim KS, Rhee JT, Lee DS, Lee JS (2008) Development of position encoding circuit for a multi-anode position sensitive photomultiplier tube. *Nucl Med Mol Imaging* (2010) 42:469–477
31. Ito M, Lee JP, Lee JS (2013) Timing Performance Study of New Fast PMTs With LYSO for Time-of-Flight PET. *IEEE Trans Nucl Sci* 60:30–37
32. Yoon HS, Ko GB, Kwon SI, Lee CM, Ito M, Song IC, Lee DS, Hong SJ, Lee JS (2012) Initial results of simultaneous PET/MRI experiments with an MRI-compatible silicon photomultiplier PET scanner. *J Nucl Med* 53:608–14

33. Ko GB, Yoon HS, Kwon SI, Song IC, Lee DS, Lee JS (2013) New high performance SiPM PET insert to 9.4-T MR scanner for simultaneous PET/MRI studies. Soc. Nucl. Med. Annu. Meet. Abstr. p 46
34. Pichler BJ, Judenhofer MS, Wehrl HF (2008) PET/MRI hybrid imaging: devices and initial results. *Eur Radiol* 18:1077–86
35. Herzog H, Pietrzyk U, Shah NJ, Ziemons K (2010) The current state, challenges and perspectives of MR-PET. *Neuroimage* 49:2072–82
36. Delso G, Ziegler S (2009) PET/MRI system design. *Eur J Nucl Med Mol Imaging* 36 Suppl 1:S86–92
37. Pichler BJ, Wehrl HF, Kolb A, Judenhofer MS (2008) Positron emission tomography/magnetic resonance imaging: the next generation of multimodality imaging? *Semin Nucl Med* 38:199–208
38. Hu Z, Ojha N, Renisch S, et al (2009) MR-based attenuation correction for a whole-body sequential PET/MR system. *IEEE Nucl. Sci. Symp. Med. Imaging Conf. Rec. IEEE*, pp 3508–3512
39. Catana C, Procissi D, Wu Y, Judenhofer MS, Qi J, Pichler BJ, Jacobs RE, Cherry SR (2008) Simultaneous in vivo positron emission tomography and magnetic resonance imaging. *Proc Natl Acad Sci U S A* 105:3705–10
40. Judenhofer MS, Wehrl HF, Newport DF, et al (2008) Simultaneous PET-MRI: a new approach for functional and morphological imaging. *Nat Med* 14:459–65
41. Maramraju SH, Junnarkar S, Ravindranath B, et al (2008) An MR compatible PET scanner based on RatCAP for small animal imaging at 9.4 T. *IEEE Nucl. Sci. Symp. Med. Imaging Conf. Rec. IEEE*, pp 3679–3682
42. Schlemmer H, Pichler B, Schmand M (2008) Simultaneous MR/PET imaging of the human brain: feasibility study. *Radiology*
43. Lee JS, Hong SJ (2010) Geiger-mode avalanche photodiodes for PET/MRI. *Electron. circuits Radiat. Detect. Boca Rat. CRC Press LLC*. pp 179–200
44. Roncali E, Cherry SR (2011) Application of silicon photomultipliers to positron emission tomography. *Ann Biomed Eng* 39:1358–77

45. Lee J (2010) Technical Advances in Current PET and Hybrid Imaging Systems. *Open Nucl. Med. J.*
46. Lee JS, Ito M, Sim KS, et al (2007) Investigation of Solid-State Photomultipliers for Positron Emission Tomography Scanners. *J Korean Phys Soc* 50:1332
47. Hong SJ, Song IC, Ito M, Kwon SI, Lee GS, Sim KS, Park KS, Rhee JT, Lee JS (2008) An Investigation Into the Use of Geiger-Mode Solid-State Photomultipliers for Simultaneous PET and MRI Acquisition. *IEEE Trans Nucl Sci* 55:882–888
48. Schaart DR, van Dam HT, Seifert S, Vinke R, Dendooven P, Löhner H, Beekman FJ (2009) A novel, SiPM-array-based, monolithic scintillator detector for PET. *Phys Med Biol* 54:3501–12
49. Olcott P, Peng H, Levin C (2009) Novel Electro-Optical Coupling Technique for Magnetic Resonance--Compatible Positron Emission Tomography Detectors. *Mol. Imaging*
50. Kolb A, Lorenz E, Judenhofer MS, Renker D, Lankes K, Pichler BJ (2010) Evaluation of Geiger-mode APDs for PET block detector designs. *Phys Med Biol* 55:1815–32
51. Kwon SI, Lee JS, Yoon HS, et al (2011) Development of small-animal PET prototype using silicon photomultiplier (SiPM): initial results of phantom and animal imaging studies. *J Nucl Med* 52:572–9
52. Yamamoto S, Imaizumi M, Watabe T, Watabe H, Kanai Y, Shimosegawa E, Hatazawa J (2010) Development of a Si-PM-based high-resolution PET system for small animals. *Phys Med Biol* 55:5817–31
53. Yamamoto S, Imaizumi M, Kanai Y (2010) Design and performance from an integrated PET/MRI system for small animals. *Ann. Nucl. ...*
54. National Electrical Manufacturers Association (2008) NEMA: Standards Publication NU 4-2008: Performance measurements for small animal positron emission tomographs (PETs). Rosslyn, VA
55. Lee JS, Park KS, Lee DS, Lee CW, Chung J-K, Lee MC (2005) Development and applications of a software for Functional Image Registration (FIRE). *Comput Methods Programs Biomed* 78:157–64
56. Kang J, Choi Y, Hong KJ, Jung JH, Hu W, Huh YS, Lim H, Kim B-T (2010) A feasibility study of photosensor charge signal transmission to

preamplifier using long cable for development of hybrid PET-MRI.  
Med Phys 37:5655

57. Yamamoto S, Watabe H, Kanai Y, Aoki M, Sugiyama E, Watabe T, Imaizumi M, Shimosegawa E, Hatazawa J (2011) Interference between PET and MRI sub-systems in a silicon-photomultiplier-based PET/MRI system. Phys Med Biol 56:4147–59
58. Renker D, Lorenz E (2009) Advances in solid state photon detectors. J. Instrum.
59. Yamamoto S, Satomi J, Watabe T, Watabe H, Kanai Y, Imaizumi M, Shimosegawa E, Hatazawa J (2011) A temperature-dependent gain control system for improving the stability of Si-PM-based PET systems. Phys Med Biol 56:2873–82
60. Hong SJ, Kim CM, Cho SM, Woo H, Ko GB, Kwon S Il, Rhee JT, Song IC, Lee JS (2011) A Feasibility Study on the Use of Optical Fibers for the Transfer of Scintillation Light to Silicon Photomultipliers. IEEE Trans Nucl Sci 58:579–589

# 국문 초록

**서론:** 고민감도, 고해상도 PET은 많은 양의 데이터가 발생되므로 이를 처리할 수 있는 고성능 DAQ가 필요하다. 대부분의 PET DAQ 장치들은 출력신호 종류, 인터페이스, 출력신호 채널의 구성 등 각 PET에 맞게 전용으로 설계된다. 본 연구에서는 양전자 단층촬영장치 (Positron emission tomography; PET)에서 사용하는 네트워크 기반 데이터획득 장치 (Data acquisition system; DAQ)를 개발하여 PET의 성능을 향상 시키고자 한다. 서로 다른 종류의 출력 신호들을 가진 다양한 PET에 쉽게 대응할 수 있도록 각PET에 적합한 입력 모듈을 이용하는 모듈형 시스템을 도입하였다. 현장 프로그래머블 게이트 어레이 (Field-programmable gate array; FPGA) 기반 신호처리와 10 기가비트 이더넷 (Gigabit Ethernet) 통신을 이용하여 확장 가능한 고성능 DAQ을 구현하였다.

**방법:** 입력 모듈, ADC 모듈, FPGA 모듈로 구성되어 있는 DAQ 장치는 PET으로부터 40개의 아날로그 입력 채널과 10개의 트리거 입력을 받을 수 있다. 데이터 전송과 DAQ확장을 위해 10 기가비트 이더넷 통신방식을 사용하였다.

**결과:** 10 기가비트 이더넷 DAQ장치를 이용하여 최대 초당 5천 6백만 사건의 PET데이터를 획득, 처리 할 수 있었다.

**결론:** 결론적으로 다양한 크기와 신호를 가지는 PET에 적용 가능

한 확장형 네트워크 기반 DAQ장치를 개발하였다. 이더넷 네트워크 기반 DAQ 장치는 최대 1만개의 입력 신호를 처리 할 수 있는 확장성을 가지게 되었다.

---

주요어 : 양전자방출단층촬영, 데이터획득장치

학 번 : 2008-22004